Delft University of Technology

The role of water-treated municipal solid waste incineration (MSWI) bottom ash in microstructure formation and strength development of blended cement pastes

Chen, Boyu; Ye, Guang

Important note
To cite this publication, please use the final published version (if applicable).
Please check the document version above.

The role of water-treated municipal solid waste incineration (MSWI) bottom ash in microstructure formation and strength development of blended cement pastes

Boyu Chen [a,*], Guang Ye [a,b]

[a] *Department of Materials and Environment (Microlab), Faculty of Civil Engineering and Geoscience, Delft University of Technology, Delft, the Netherlands*
[b] *Magnel-Vandepitte Laboratory, Department of Structural Engineering and Building Materials, Ghent University, 9052 Ghent, Belgium*

A B S T R A C T

This research explored the microstructure formation and strength development of blended cement pastes prepared with municipal solid waste incineration (MSWI) bottom ash. A new sample preparation approach involving water treatment of MSWI bottom ash was developed to prevent sample cracking caused by the presence of metallic aluminum (Al) in bottom ash. The result showed that ions released during water treatment of MSWI bottom ash delayed cement hydration but promoted ettringite formation in blended cement pastes during the first day. Due to water treatment, the compressive strength of MSWI bottom ash blended cement paste increased to a level similar to that of Class F coal fly blended cement paste after 28 days. Blending water-treated MSWI bottom ash (WMBA) with cement promoted clinker hydration at later stages. The reaction products of WMBA in blended cement system were C-S-H gel and sodicgedrite, which contributed to strength development by filling the capillary pores.

1. Introduction

Improper management of municipal solid waste will have a huge impact on the environment and human health [1]. Waste incineration, when equipped with an effective air pollution control system, is considered a sustainable method of waste disposal [1,2]. Waste-to-energy plants burn waste as a fuel source for power generation, greatly reducing the quantities of waste that need to be landfilled [3–5]. Over the past few decades, there has been a continuous increase in the number of waste-to-incineration plants [6]. The widespread adoption of waste incineration makes the disposal of incineration residue an urgent issue. The primary residue generated from waste incineration is the ash collected at the bottom of the incinerator, often referred to as municipal solid waste incineration (MSWI) bottom ash [7,8].

Previous studies indicate that MSWI bottom ash has the potential to be used as supplementary cementitious material (SCM), especially as an alternative to Class F coal fly ash [6]. This is because the chemical composition of MSWI bottom ash falls within a similar range as that of Class F coal fly ash [6], and the pozzolanic reactivity of MSWI bottom ash can be close to that of Class F coal fly ash [9,10]. However, although MSWI bottom ash is as reactive as Class F coal fly ash, it is difficult to

achieve equal strength level when using equivalent amount of MSWI bottom ash and Class F coal fly ash to prepare blended cement pastes. This difficulty typically stems from the presence of metallic aluminum (Al) in MSWI bottom ash [11–15], which will oxidize upon its contact with the alkaline pore solution of blended cement pastes. The hydrogen gas released after the redox reaction of metallic Al can significantly reduce the compressive strength of cement pastes blended with MSWI bottom ash [16]. Therefore, it is crucial to decrease the metallic Al content in MSWI bottom ash before its substitution for Portland cement.

For the application as SCM, it is recommended to reduce the metallic Al content of MSWI bottom ash through water treatment rather than NaOH solution treatment to avoid the introduction of excessive alkali ions into blended cement system [6]. Currently, there is no generally accepted procedure for water treatment. The oxidation rate of metallic Al in water can be influenced by factors such as the particle size of MSWI bottom ash, the pH in the mixture of MSWI bottom ash and water, the temperature of the environment, and the duration of treatment [17,18]. The time required for complete oxidation of metallic Al in water varies significantly. The metallic Al content of MSWI bottom ash exhibits a slow decrease when water treatment is conducted at room temperature [18]. The reaction of metallic Al can be accelerated by raising the

---

* Corresponding author.
  E-mail address: B.Chen-4@tudelft.nl (B. Chen).

Development of blended cement pastes using MSWI bottom ash as supplementary cementitious materials (SCM)
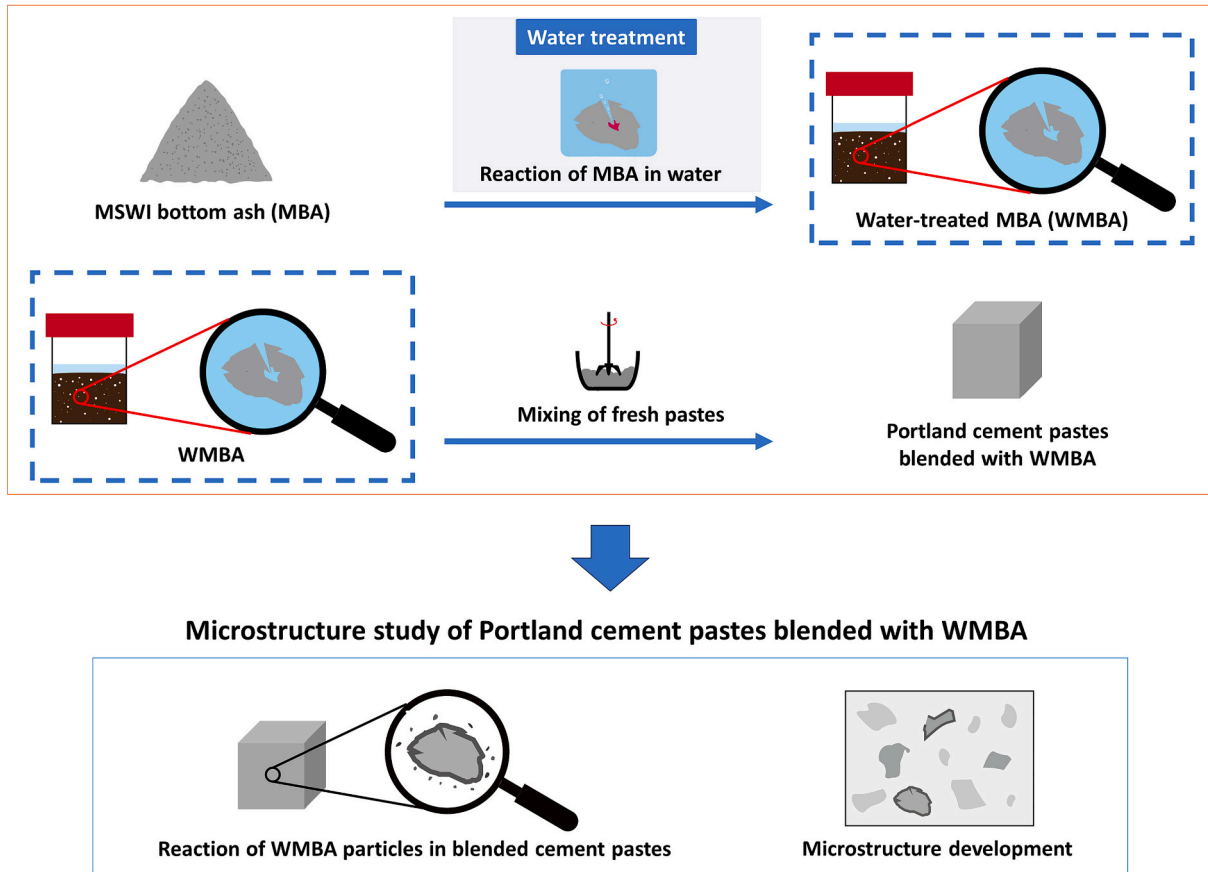

Fig. 1. Outline of this research.

temperature from room temperature to 105 °C [17] or by reducing the particle size of MSWI bottom ash to 3 μm [18]. However, these two approaches are both energy-intensive. It is worth noting that previous studies mainly focused on the effectiveness and efficiency of water treatment on metallic Al content reduction [6]. The development of sustainable water treatment methods remains a task that requires continuous research and exploration. Additionally, there is a lack of investigation into how water treatment of MSWI bottom ash influences the microstructure formation of blended cement pastes.

Previous researchers mainly studied the effects of MSWI bottom ash addition on cement hydration using calorimetry [16,17,19–22]. The contribution of MSWI bottom ash to the microstructure development of hardened pastes remains largely unexplored. The microstructure of hardened cement paste strongly influences its mechanical properties, volume stability, and durability, thereby playing a crucial role in determining the application of developed cement products [23]. Currently, when MSWI bottom is used as SCM, the compressive strength is the main criterion considered during mix design [24]. A comprehensive examination of the reaction process and the reaction products of MSWI bottom ash in blended cement pastes would provide a theoretical basis for the wide application of MSWI bottom ash as SCM.

Fig. 1 provides a visual outline of this study. The objective of this study is to investigate the reaction process and reaction products of MSWI bottom ash as SCM, and thus provide insights into the microstructure formation and strength development of blended cement pastes prepared with MSWI bottom ash. A new paste sample preparation strategy, which involves water treatment of MSWI bottom ash, is developed to eliminate the occurrence of expansive cracks in MSWI

bottom ash blended cement pastes caused by metallic Al. To provide a thorough understanding of water treatment, the mechanism of water treatment on metallic Al content reduction, the reaction of MSWI bottom ash during water treatment, and subsequent impact of water treatment on the microstructure formation of blended cement pastes are studied. The effects of water-treated MSWI bottom ash (WMBA) on cement hydration, reaction product formation, and strength development are elucidated by comparing WMBA blended cement paste with plain cement paste and micronized sand blended cement paste.

2. Materials and methods

2.1. Materials

The materials used in this work include Portland cement (PC), MSWI bottom ash (MBA), Class F coal fly ash (FA), and micronized sand (M300). The PC is CEM I 52.5 R, produced by ENCI (the Netherlands). The MBA was in the form of fine powder and obtained after mechanical treatments of MSWI bottom ash aggregates. The MSWI bottom ash aggregates were collected from a Dutch waste-to-energy plant. More detailed information about the mechanical treatments and MSWI bottom ash aggregates could be found in our previous publication [25]. The FA supplied by *Vliegasunie B.V.* and the M300 provided by SIKRON® were each used as a reference for MBA. This is because the pozzolanic reactivity of FA was found to be similar to that of MBA [10], and the M300 is a chemically inert quartz powder with particle size in the same range as MBA.

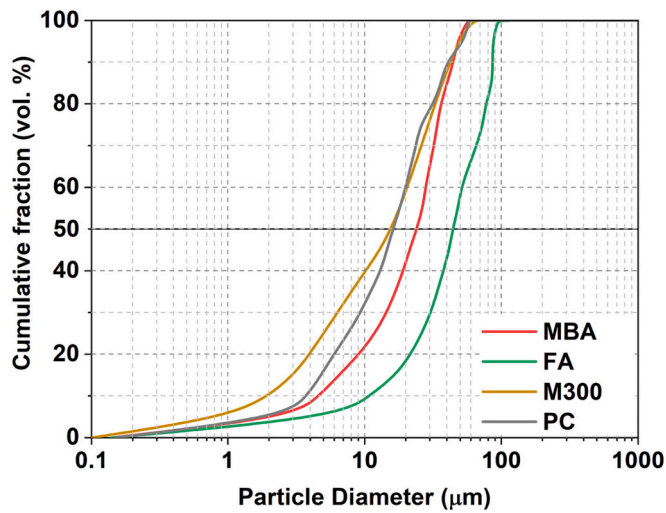The particle size distribution of PC, MBA, FA and M300 was

Fig. 2. Particle size distribution of MBA, FA, M300, and PC, determined by laser diffraction method.

measured using the laser diffraction method (EyeTech S/N 60298). As shown in Fig. 2, the D_{50} of M300 was 17 μm, almost the same as that of PC. The D_{50} of MBA is 24 μm, smaller than that of FA (44.2 μm). Compared with MBA and FA, the particle size of M300 was smaller. It was difficult to find commercially available micronized sand with the same particle size as MBA. M300 was the one that has particle size distribution most similar to MBA.

Table 1 provides information about the chemical compositions of PC, MBA, and FA. The mineralogical compositions of PC, FA, and MBA can be found in Table 2, Table 3, and Table 6, respectively. The chemical composition was acquired via the X-ray fluorescence (XRF). The quantitative X-ray diffraction (QXRD) analysis was conducted to determine the mineralogical composition [10]. The detailed analysis about the composition and the reactivity of MBA and FA can be found in our previous work [10].

2.2. Mix design

According to the findings of our previous research, the pozzolanic reactivity of MBA is similar to that of FA, the mix design of Portland cement blended with MBA can refer to the experience with Portland cement blended with Class F coal fly ash [10]. Since the percentage of coal fly ash added as SCM in concretes usually ranges from 15 wt% to 35 wt% [26], the percentages of PC replaced by MBA in blended cement were chosen to be the same. The heavy metal contents in blended cement system will increase with the addition of MBA. The low percentage of MBA in blended cement also prevents the leaching of contaminants into the environment. Table 4 provides detailed information about the mix design used in this work. The water-to-binder ratio is the same for all mixtures (0.4). The binder includes PC and supplementary cementitious materials (SCMs).

In total, five series of paste samples were prepared: 100 CEM, FA CEM, M300 CEM, MBA CEM, and WMBA CEM. The specific details of each series are shown in Table 4. 100 CEM, FA CEM, and M300 CEM are reference paste samples. 100 CEM was made by mixing PC with water. FA CEM and M300 CEM are pastes of Portland cement blended with FA

and M300, respectively. MBA CEM and WMBA CEM are blended cement pastes made from the same raw materials (Portland cement and MBA) but following different sample preparation procedures. The percentages of FA, M300, and MBA added in blended cement are 15 %, 25 %, and 35 % by weight.

Table 2
Mineralogical composition of PC (CEM I 52.5 R) determined by QXRD analysis.

Phases	wt%	Formula	ICSD code
Alite (C_3S)	66.1	Ca_3SiO_5	94,742
Belite(C_2S)	15.5	Ca_2SiO_4	963
C_3A_{cubic}	2.1	$Ca_9(Al_2O_6)_3$	1841
$C_3A_{orthorombic}$	2.9	$Al_{5.176}Ca_{8.393}Fe_{0.46}Na_{0.875}O_{18}Si_{0.375}$	100,220
C_4AF	6.9	Ca_2FeAlO_5	51,265
Calcite	0.8	$CaCO_3$	80,869
Mayenite	1.3	$Ca_{12}Al_{14}O_{33}$	6287
Bassanite	0.6	$Ca(SO_4)(H_2O)_{0.5}$	380,286
Anhydrite	1.2	$CaSO_4$	16,382
Quartz	0.4	SiO_2	174
Arcanite	1.4	K_2SO_4	79,777
Amorphous phase	1.0	–	–
Sum	100	–	–

Table 3
Mineralogical composition of FA determined by QXRD analysis.

Phases	Proportions (wt %)	Formulae	ICSD codes
Quartz	11.5	SiO_2	156,198
Mullite	11.7	$Al_{2.24}Si_{0.76}O_{4.88}$	313,794
Hematite	0.5	Fe_2O_3	2,070,090
Lime	0.1	CaO	1,503,123
Calcite	0.2	$CaCO_3$	1,611,066
Hexapotassium hexaoxodiferrate	0.1	$K_6(Fe_2O_6)$	16,534
Iron(III) oxide hydroxide	1.3	$FeO(OH)$	94,874
Periclase	0.3	MgO	1,110,749
Wadsleyite	0.3	$Mg_{1.84}Fe_{0.16}SiO_4$	66,491
Amorphous phase	74.0	–	–
Sum	100	–	–

Table 4
Mix design of the paste samples.

Paste samples	Raw materials (wt%)				Water-to-PC ratio	Water-to-binder ratio
	FA	MBA	M300	PC		
100 CEM	–	–	–	100	0.4	
15 FA CEM	15	–	–			
15 MBA CEM	–	15	–	85	0.47	
15 WMBA CEM*	–	15	–			
25 FA CEM	25	–	–			
25 MBA CEM	–	25	–			
25 WMBA CEM*	–	25	–	75	0.53	0.4
25 M300 CEM	–	–	25			
35 FA CEM	35	–	–			
35 MBA CEM	–	35	–	65	0.62	
35 WMBA CEM*	–	35	–			

* The water treatment of MBA was included in the sample preparation process.

Table 1
Chemical compositions of PC, MBA, and FA determined by XRF analysis.

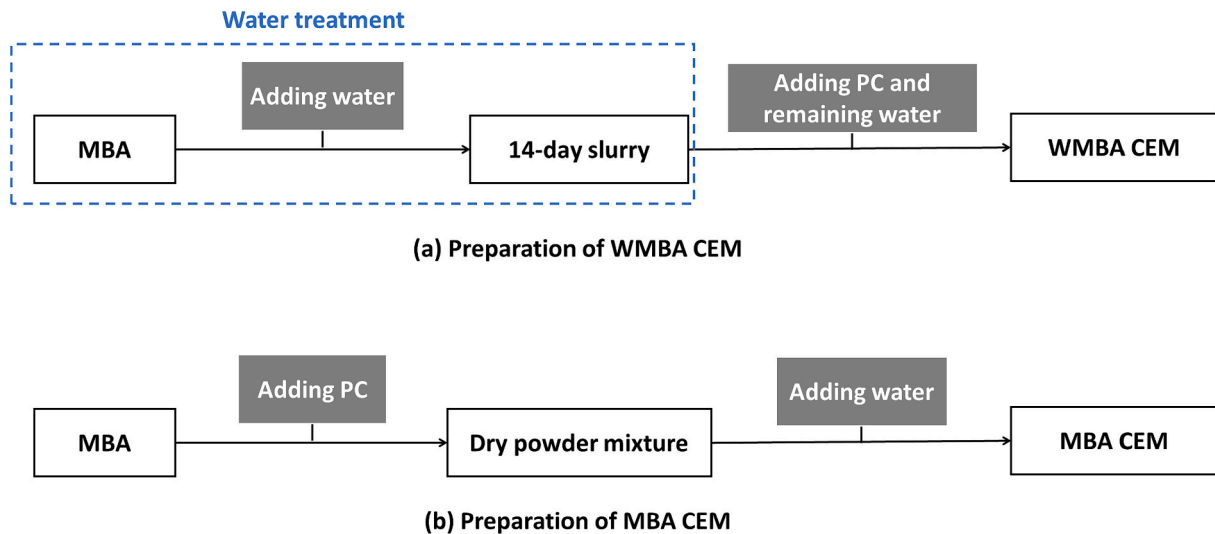| Compounds (wt%)	SiO_2	CaO	Al_2O_3	Fe_2O_3	Na_2O	K_2O	SO_3	Cl	MgO	Others	LOI_{550}	Sum
PC	20.58	63.74	4.74	2.47	0.36	0.71	3.07	0.10	2.76	1.32	0.16	100
MBA	52.91	13.44	10.18	9.29	4.24	0.84	0.7	0.27	2.4	3.56	2.17	100
FA	55.29	4.43	25.03	6.94	0.91	1.66	0.73	0.01	1.41	2.67	0.92	100

Fig. 3. Illustration of the sample preparation process of (a) WMBA CEM and (b) MBA CEM. The FA CEM and M300 CEM are prepared in the same way as MBA CEM.
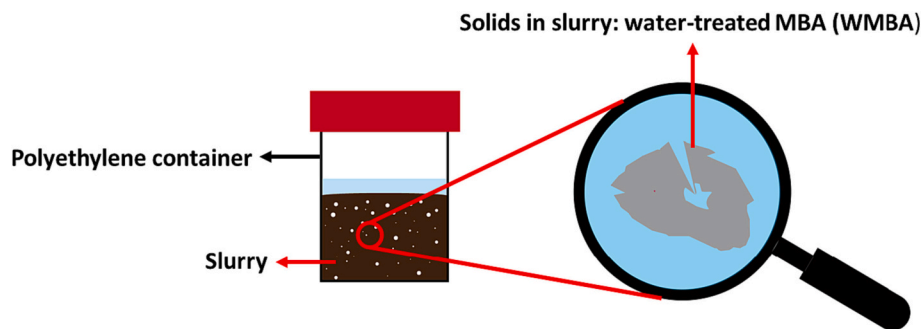

Fig. 4. illustration of water treatment of MBA.

2.2.1. Samples preparation

Fig. 3 (a) demonstrates the sample preparation procedure of WMBA CEM. The water used to prepare WMBA CEM was divided into two portions. One portion was used to treat MBA prior to the addition of PC. The remaining water was added when mixing the fresh pastes. The aim of water treatment is to oxidize the metallic Al embedded in MBA. The deionized water was mixed with MBA at a mass ratio of 0.4. The mixture obtained was named "slurry" in this context. As shown in Fig. 4, the slurry was sealed in a polyethylene container at room temperature (between 22 and 25 °C). The solids in the slurry are called *water-treated MBA (WMBA)*.

The water treatment lasted until the metallic Al content in WMBA reached the lowest achievable value. The metallic Al content in WMBA at different time intervals of water treatment was monitored by measuring the metallic Al content in the slurry with the water displacement method described in our previous publication [25]. Considering the low metallic Al content in the slurry, around 140 g of the slurry, which contains 100 g WMBA, was used for each measurement. The hydrogen gas collected during the measurement of 140 g slurry equals the hydrogen gas released by the metallic Al present in 100 g WMBA. With the volume of released hydrogen gas, the metallic Al content in WMBA can be calculated. In the end, the water treatment lasted for 14 days to achieve the lowest level of metallic Al in WMBA. The obtained slurry, also named 14-day slurry, was mixed with PC and the remaining water to make WMBA CEM.

The raw materials used to prepare MBA CEM are the same as that of WMBA CEM. However, the sample preparation procedure of MBA CEM differs from that of WMBA CEM. As illustrated in Fig. 3 (b), for the preparation of MBA CEM, the MBA was first blended with PC.

Afterward, the dry powder blends were directly mixed with water to prepare MBA CEM. FA CEM and M300 CEM were prepared following the same procedure as MBA CEM. 100 CEM was prepared by directly mixing PC with water.

All the fresh pastes were mixed for 4 min with a high-shear mixer (model IKA® T 50 ULTRA-TURRAX®) and then cast in the mold with the dimension of $20 \times 20 \times 20$ mm^3. The paste specimens were first cured at room temperature for 24 h. After demolding, the specimens were sealed with cling film and cured in a fog room (20 °C, 99 % RH) until the test ages.

2.2.2. Studies of reaction between MBA and water

The dissolution of MBA during water treatment was studied by measuring the pH and elemental concentration of the liquid in the slurry at time intervals of 1 day, 7 days, and 14 days. The slurry tested at each time interval was prepared by mixing 500 g of MBA with 200 g of water. The liquid in the slurry was filtered through Whatman™ 42 filter paper with a pore size of 1.1 μm. The pH of filtered liquid was measured with a pH meter from Metrohm (model 827). The pH meter was calibrated with buffer solution with pH of 7 and 10.01 produced by HACH®. The filtered solutions were diluted with nitric acid (0.2 vol%) or sodium hydroxide solution (0.1 mol/L). It is worth mentioning that the sodium hydroxide solution was only used for dilution when measuring the concentration of sulfur in the filtered solution. The diluted solutions were analyzed through inductively coupled plasma-optical emission spectroscopy (ICP-OES), model PerkinElmer Optima 5300DV.

The reaction of MBA in the process of water treatment was also investigated by measuring the reaction heat with a TAM-AIR-314 isothermal conduction calorimeter. Around 10 g of slurry, after being
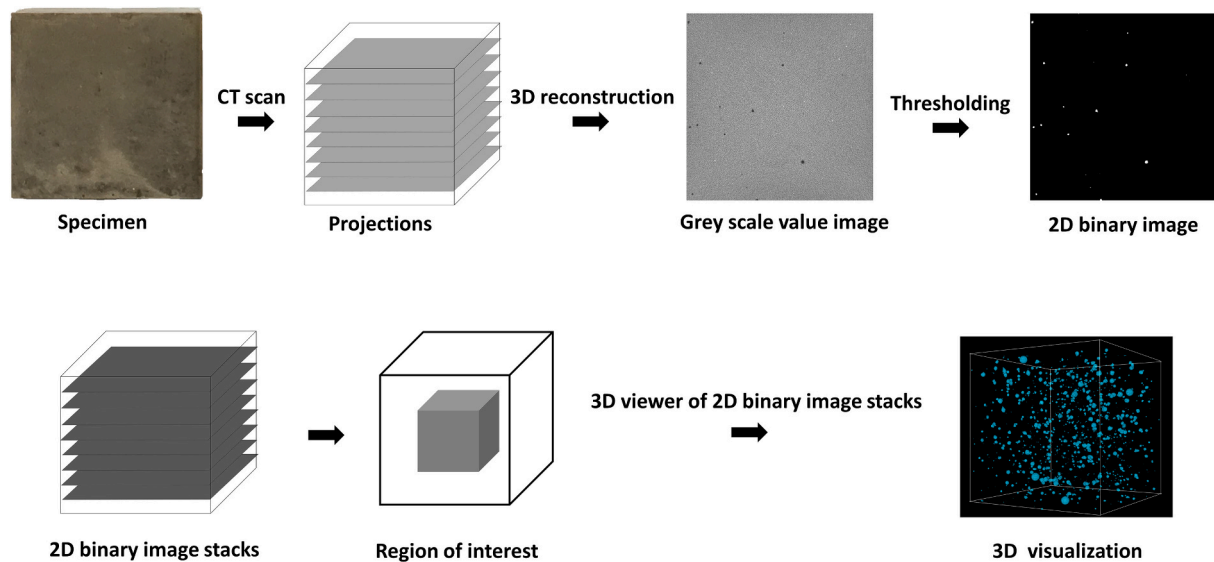
Fig. 5. The image analysis process of the projections obtained after the CT scan of 1-day paste sample. The terms "2D" and "3D" in this image stand for "two-dimensional" and "three-dimensional" respectively. This image demonstrates the transformation from planar imaging to volumetric visualization.

poured and sealed in a glass ampoule, was loaded in the calorimeter. The temperature of the calorimeter was controlled at 20 °C.

After water treatment, the 14-day slurry was dried in a vacuum freeze-dryer (−24 °C and 0.1 Pa) for more than three months to remove the water in WMBA. After drying, the mineralogical composition of WMBA was measured with X-ray diffraction (XRD). The QXRD analysis was performed to quantify the contents of the phases present in WMBA. The molecular structure of WMBA was studied by identifying its chemical bonds with Attenuated Total Reflectance-Fourier Transform Infrared (ATR-FTIR) spectroscopy (model Perkin Elmer Spectrum 100). The measurement covers the wavenumber from 600 to 4000 cm^{-1}, and the resolution is 1 cm^{-1}.

2.2.3. Paste sample characterization

2.2.3.1. Compressive strength measurements. The compressive strength of cubic paste samples (20 × 20 × 20 mm^3) was measured for 100 CEM, FA CEM, MBA CEM, WMBA CEM, and M300 CEM, at the curing ages of 1 day, 7 days, 28 days, and 90 days. The test procedure was the same as that described in NEN-EN 196–1:2016 [27]. The compressive strength was determined by calculating the arithmetic mean of 12 repeated test results at each curing age.

2.2.3.2. X-ray computed tomography (CT) scan. The X-ray computed tomography scan is a non-destructive testing technique that can be used to examine whether the metallic Al in MBA and WMBA causes cracking inside MBA CEM and WMBA CEM. The corrosion of metallic Al is very fast at the pH of cement pore solution [18]. The hydrogen gas released by the reaction of metallic Al in Portland cement pastes blended with MSWI bottom ash could cause volume expansion before setting [18] or even cracking upon hardening [16]. Given that the damage induced by the corrosion of metallic Al usually occurred within the first day, the 1-day cubic samples prepared for the strength measurement were scanned using a Phoenix Nanotom Micro-CT scanner. During scanning, the samples were sealed with plastic film to prevent drying. The X-ray source tube worked at 120 kV and 130 μA, and the voxel resolution was 15 μm^3.

The image analysis process of the projections obtained after CT scan is shown in Fig. 5. The three-dimensional (3D) reconstruction of acquired projections was carried out with the software Phoenix Datos|x Reconstruction 2.0 to obtain greyscale value images. ImageJ, an image processing program, was used to process the greyscale value images. The pores and cracks were segmented using the triangle thresholding algorithm proposed by Zack et al. [28]. After the thresholding operation, the two-dimensional (2D) binary images were created from the greyscale value images. The 2D binary image stacks were visualized with the ImageJ 3D viewer [29]. The region of interest was the cube of edge 12 mm located in the center of the specimen. A 3D image of the binary image stacks for this cube was used to illustrate the spatial distribution of the pores and cracks in MBA CEM and WMBA CEM.

2.2.3.3. Pore solution analysis. Comparing the ion concentrations in the pore solution derived from 1-day paste samples of WMBA CEM and M300 CEM can provide insight into the reaction of WMBA in blended cement within the first day of reaction. The samples used for pore solution extraction were prepared in the same way as those used for strength measurement. The only difference is the size of the mold. The pastes were cast and sealed in polyethylene bottles with a diameter of 35 mm and a height of 70 mm. The pore solution of 1-day hardened pastes was extracted by the steel die method [30] using pressure up to 300 MPa. The extracted solution was immediately filtered through Whatman™ 42 filter paper. The pH and the elemental concentration of filtrated solution were determined by pH meter and ICP-OES spectrometer, respectively, in the same way as for the analysis of the liquid part of the slurry (Section 2.2.2). The elements under consideration are Ca, Na, K, Mg, Si, Al, Zn, Fe, and S.

2.2.3.4. Isothermal calorimetry. Isothermal calorimetry was used to study the hydration kinetics. The heat flow of the hydration during the first eight days was measured by TAM-AIR-314 isothermal conduction calorimeter. The fresh pastes were prepared the same way as that used for the strength measurements. The tests were performed at 20 °C following the ASTM C1697 [31].

2.2.3.5. Hydration stoppage. The hydration process was stopped using the solvent exchange method. The fresh pastes were cast and sealed in polyethylene bottles (d = 35 mm, h = 70 mm). The curing condition was the same for the samples prepared for strength measurement. After curing for 1 day, 7 days, 28 days, and 90 days, the hardened pastes were demolded and cut into slices with a diameter of 35 mm and a thickness of 2 mm. These slices were immersed in isopropanol for 7 days, during which the isopropanol was refreshed after 24 h. After 7 days of
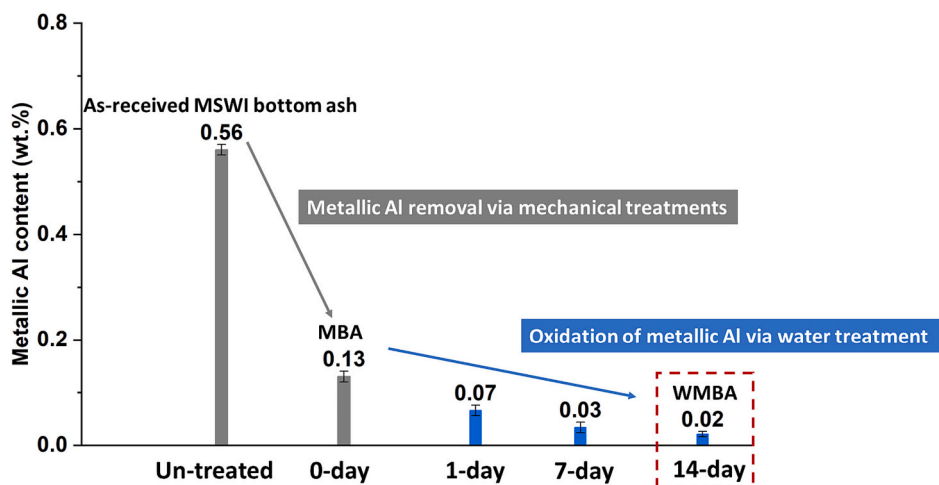
Fig. 6. The changes of metallic Al content after mechanical treatments and water treatment. The metallic Al was separated from as-received MSWI bottom ash by sieving during the mechanical treatments. Due to water treatment, the metallic Al in MBA transformed into the oxidized form.

immersion, the slices were dried and stored in a low-humidity, low-vacuum desiccator.

The dried slices were directly used to prepare test samples for scanning electron microscopy (SEM) and nitrogen adsorption tests. The dried slices were manually ground into powder using mortar and pestle to prepare the samples for XRD analysis and thermogravimetric analysis (TGA). Before grinding, the layer on the surface of dried slices was removed by dry polishing with sandpaper. The polishing and grinding were performed in a glove box under N_2 atmosphere to prevent carbonation.

2.2.3.6. X-ray diffraction analysis. The XRD analysis was used to identify the newly formed crystalline products. The changes in the contents of the crystalline and amorphous phases in hardened pastes with curing ages were determined by QXRD analysis. Silicon powder was used as internal standard to mix with test powder samples. The experiments and the analysis of obtained XRD spectra were performed in the same way as that described by Chen et al. [10].

2.2.3.7. Thermogravimetric analysis. The reaction of SCMs in blended cement is usually accompanied by the consumption of portlandite [32]. The portlandite content in hardened cement pastes at different curing ages was determined by TGA. The thermal analyzer NETZSCH STA 449 F3 Jupiter® was used for the analysis. The experiment was performed under argon atmosphere. The temperature increased from 40 to 1000 °C at a rate of 10 °C/min. The weight loss of $Ca(OH)_2$ ($WL_{Ca(OH)_2}$) was determined using the tangential method described in [33]. The amount of portlandite in 100 g of anhydrous paste sample was determined following the equation : $Ca(OH)_{2,anhydrous} = \frac{WL_{Ca(OH)_2} \times \frac{74}{18}}{\text{weight at } 600°C}$.

2.2.3.8. Scanning electron microscopy. The hydration products in 90-day hardened pastes samples were analyzed using FEI QUANTA FEG 650 ESEM. After being mounted in epoxy resin, the samples were ground and polished with pure ethanol ($\geq 96\%$ v/v, TechniSolv®) as lubricant. The polished samples were coated with a thin layer of carbon (around 10 nm) to improve their conductivity under a high vacuum. The electron beam voltage and working distance were set at 15 kV and 10 mm, respectively. The hydration products were observed by backscattered electron (BSE) imaging in scanning electron microscopy (SEM). The chemical composition of the hydration products was measured with integrated Energy Dispersive X-rays spectroscopy (EDS) detector. The spot analysis was performed at around 200 manually selected locations in the region of hydration products. It is worth mentioning that the inner

products that form rims around the unhydrated cement grains were not measured. The settings of the measurements and the selection of measured locations follow recommendations proposed by Rossen et al. [34].

2.2.3.9. Porosity measurements. The porosity in 90-day hardened pastes was analyzed using nitrogen adsorption tests. The test was conducted by using Gemini VII 2390. The pore volume and size were determined according to the Barret-Joyner-Halenda model [35].

3. Results and discussion

3.1. Water treatment of MBA

3.1.1. Effectiveness of water treatment on metallic Al content reduction

Water treatment was applied to MBA to reduce its metallic Al content. As illustrated in Fig. 6, the MBA obtained after the mechanical treatments of as-received MSWI bottom ash contains an average of 0.13 wt% metallic Al. The metallic Al content decreased by 46 % within the first day of water treatment. The decrease of metallic Al content became slower with the prolonging of water treatment. From the 7th to the 14th day, the metallic Al content only decreased by around 0.01 wt%. After 14 days, the metallic Al content was reduced by 85 %, reaching 0.02 wt % in WMBA.

The duration of water treatment was set at 14 days because the corrosion of the residual metallic Al in water was slower in later stages. The reaction products of metallic Al and water can function as protective layers to inhibit further corrosion of metallic Al. After 14 days of water treatment, the metallic Al content in WMBA was minimal. When water treatment was prolonged to >14 days, it became more difficult to detect the change of metallic Al content by water displacement method.

3.1.2. Mechanism of water treatment on metallic Al oxidation

The mechanism underlying water treatment-induced oxidation of metallic Al in MBA was investigated through an analysis of reaction products and an exploration of the factors influencing the corrosion of metallic Al. The types of reaction products formed after the reaction of metallic Al and water largely depend on temperature [36]. Possible reaction products of metallic Al and water are $Al(OH)_3$ (Eq. 1), $AlOOH$ (Eq.2), and Al_2O_3 (Eq. 3) [36]. At the temperature between room temperature and 280 °C, the formation of $Al(OH)_3$ is thermodynamically favored over $AlOOH$ and Al_2O_3 [36]. Since the water treatment of MBA was performed at room temperature, the reaction between metallic Al and water will produce $Al(OH)_3$ and hydrogen gas.
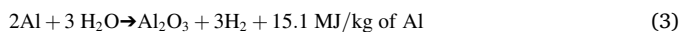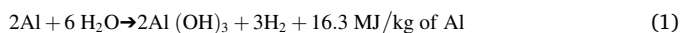
Table 5

The pH and elemental concentrations of the liquid filtered from the slurry during the water treatment.

Water treatment intervals	pH	Concentration (mg/L)								
		Ca	Na	K	Mg	Si	Al	Zn	Fe	S
1 day	8.14	833	749	142	45.3	2	1.1	<0.1	0.3	836
7 days	8.12	840	860	155	45.7	2.1	0.8	<0.1	<0.1	882
14 days	8.33	845	966	165	43.4	2.3	0.4	<0.1	<0.1	860

Table 6

Mineral phases present in MBA and WMBA and QXRD analysis results.

Phases	MBA (wt%)	WMBA (wt%)	Formula	ICSD code
Quartz	12.1	12.1	SiO_2	541,929
Cristobalite	0.4	0.4	SiO_2	1,251,919
Magnetite	0.9	0.9	Fe_3O_4	92,356
Hematite	0.4	0.4	Fe_2O_3	453,828
Wustite	0.2	0.2	FeO	309,924
Gehlenite	2.8	2.8	$Ca_2Al_2SiO_7$	1,411,155
Albite	1.9	1.1	$NaAlSi_3O_8$	1,402,109
Orthopyroxene	1.4	0.9	$Ca_{0.02}Mg_{0.30}Fe_{0.68}SiO_3$	1,615,622
Diopside	4.4	4.0	$CaMg_{0.69}Fe_{0.31}Si_2O_6$	77,809
Wollastonite	2.6	2.6	$CaSiO_3$	1,253,098
Calcite	2.1	2.2	$CaCO_3$	1,611,066
Halite	0.4	0.3	NaCl	311,644
Phosphammite	1.1	1.1	$H(NH_4)_2(PO_4)$	1,401,715
Corundum	0.7	0.7	Al_2O_3	527,601
Goethite	0.4	0.4	FeO(OH)	71,810
Gibbsite	0.2	0.2	$Al(OH)_3$	1,005,040
Iron	0.1	0.1	Fe	1,503,158
Amorphous phase	68.1	69.7	–	–
Sum	100	100	–	–

$$2Al + 6\,H_2O \rightarrow 2Al\,(OH)_3 + 3H_2 + 16.3\,MJ/kg\ of\ Al \qquad (1)$$

$$2Al + 4\,H_2O \rightarrow 2AlOOH + 3H_2 + 15.5\,MJ/kg\ of\ Al \qquad (2)$$

$$2Al + 3\,H_2O \rightarrow Al_2O_3 + 3H_2 + 15.1\,MJ/kg\ of\ Al \qquad (3)$$

The liquid filtered from the slurry was tested to be alkaline (see Table 5). This alkaline condition, which is beneficial to the corrosion of metallic Al, was created through the dissolution of MBA during water treatment. The pH of filtered liquid increased slightly when water treatment lasted from 1 day to 14 days. It is worth mentioning that the measuring accuracy of pH is ±0.003 [37]. The increased pH of filtered liquid suggests a continuous formation of $Al(OH)_3$ during water treatment because the dissociation of the $Al(OH)_3$ in water releases OH^-. This test result is consistent with that reported by Teng et al. [38], who found the pH of the solution increased after the reaction of metallic Al with water.

As shown in Table 6, halite (NaCl) was detected in the XRD measurement of MBA. The halite in MBA may facilitate the corrosion of metallic Al during water treatment. The concentration of Na^+ increased with time during water treatment (see Table 5), indicating a continuous dissolution of MBA. With the dissolution of MBA, halite releases Na^+ and Cl^- ions into the slurry. The Cl^- ions provided by halite could easily penetrate the aluminum oxide film to reach the surface of metallic Al, causing the corrosion pitting of metallic Al and thus accelerating the corrosion of metallic Al [39].

3.1.3. Reaction of MBA during water treatment

The reaction of MBA during water treatment was investigated by recording heat flow. There are two peaks in the heat evolution rate curve (Fig. 7 (a)). Fig. 7 (a) shows that the first peak appeared at 0.0016 day (2.3 min). This peak can be attributed to the wetting and dissolution of MBA in water. After the first peak, the second peak was observed at 0.14 day (see Fig. 7 (c)). The appearance of the second calorimetric peak is

mainly due to the reaction between metallic Al and water.

For the water treatment of MBA, the water to MBA mass ratio is 0.4. Thus, the MBA used to prepare 1 g of slurry for water treatment is 0.71 g. After 1 day of water treatment, the metallic Al content decreased by 0.06 wt% relative to the mass of MBA (Fig. 6), which means 0.00043 g metallic Al in the slurry was reacted. Considering the reaction of 1 g of metallic Al with water will generate 16.3 kJ (Eq. 1), the heat released after 0.00043 g of metallic Al reacting with water will be 7 J. This calculated value is only slightly lower than the total heat (8.1 J) recorded from the beginning (0.09 day) to the end (0.6 day) of the second calorimetric peak (see Fig. 7 (d)).

3.1.4. Composition change induced by water treatment

The changes in the mineralogical composition and the molecular structure of MBA were examined after water treatment. The XRD and the FTIR patterns of WMBA and MBA are presented in Fig. 8. The XRD and FTIR spectra of WMBA are almost the same as that of MBA. The peaks in the XRD spectrum of WMBA are also identified in the XRD measurement of MBA (Fig. 8(a)). Although $Al(OH)_3$ is expected to form after the metallic Al in MBA reacted with water, the gibbsite content remained unchanged (0.2 wt%) after water treatment (Table 6). There are two possible explanations for this QXRD result. First, the increase in the gibbsite content is too small to be detected by XRD. Second, the $Al(OH)_3$ formed after water treatment is semi-crystalline or has an amorphous structure. Compared with the FTIR spectrum of WMBA, the bands detected in MBA did not change their shape or location after the water treatment (Fig. 8 (b)). According to the results of XRD and FTIR analysis, water treatment of MBA did not lead to a significant change in its mineralogical composition and molecular structure.

The subtle changes in the contents of mineral phases are detectable through QXRD analysis. According to the QXRD results illustrated in Table 6, water treatment changed the contents of the amorphous phase, calcite, albite, diopside, orthopyroxene, and halite. The contents of the amorphous phase and calcite in WMBA are slightly higher than in MBA. The higher amount of amorphous phase in WMBA indicates that amorphous phase can be the reaction product formed after water treatment, such as $Al(OH)_3$ with a semi-crystalline or amorphous structure. The increase in the calcite content may result from the precipitation of the Ca^{2+} ions released by MBA during water treatment (Table 5). Compared with MBA, WMBA contains a smaller amount of albite, diopside, orthopyroxene, and halite. The decrease in the contents of these phases can be attributed to their dissolution during water treatment [40–42].

3.2. Effectiveness of water treatment in improving compressive strength of blended cement pastes prepared with MBA

As shown in Fig. 9 (a), the 28-day compressive strength of WMBA CEM is much higher than that of MBA CEM. This result indicates that the water treatment of MBA facilitates the strength improvement of blended cement pastes prepared with MBA. The main difference between MBA and WMBA is the metallic Al content. The water treatment caused little changes to the mineralogical compositions and molecular structure of MBA (see Section 3.1.4). Therefore, the higher compressive strength of WMBA blended Portland cement pastes is mainly due to the lower metallic Al content in WMBA.

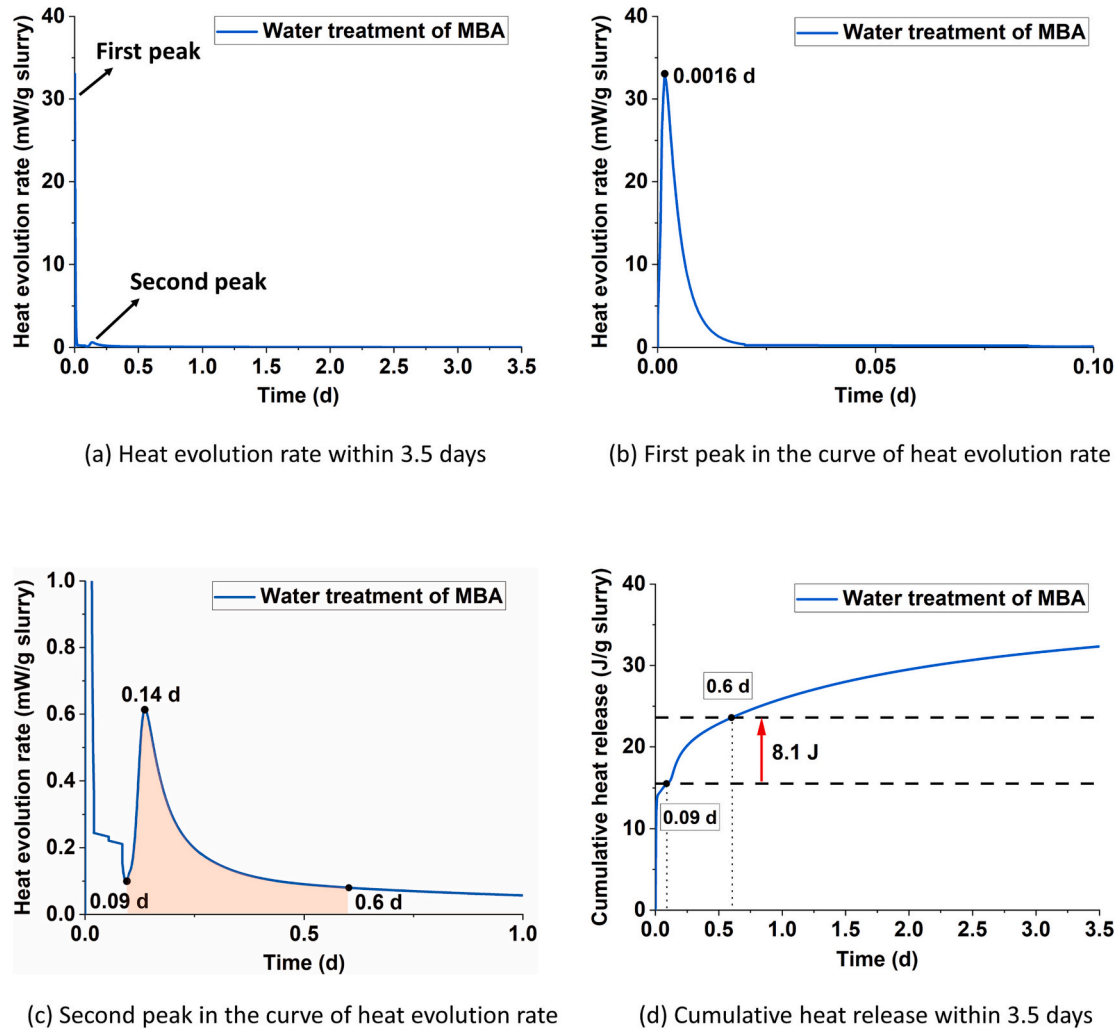The 28-day and 90-day compressive strength of WMBA CEM are

(a) Heat evolution rate within 3.5 days

(b) First peak in the curve of heat evolution rate

(c) Second peak in the curve of heat evolution rate

(d) Cumulative heat release within 3.5 days

Fig. 7. (a)-(c) Heat evolution rate and (d) cumulative heat release during water treatment of MBA.
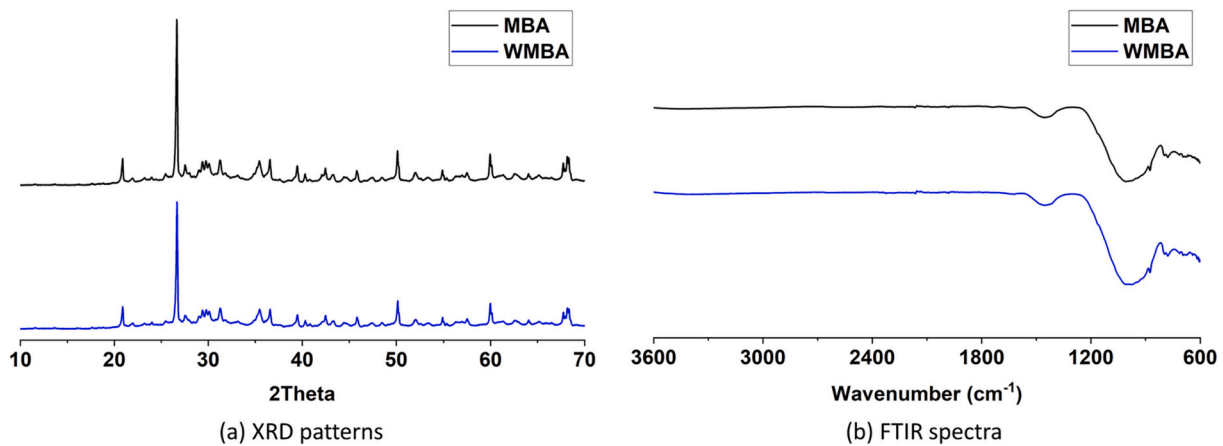

(a) XRD patterns

(b) FTIR spectra

Fig. 8. (a) XRD spectra and (b) FTIR spectra of WMBA and MBA.

close to that of FA CEM when the replacement level is between 15 wt% and 35 wt% (Fig. 9). This finding suggests that MBA, after water treatment, can be used as an alternative to FA in blended cement. It is worth noting that the 28-day 15 WMBA CEM is stronger than the 28-day 15 FA CEM. Although the reactivity of FA is similar to MBA, the particle size of FA is larger than MBA. The lower 28-day strength of 15 FA CEM can be

attributed to the slower reaction rate of FA at room temperature. The contribution of FA to strength development is more significant at later ages. The compressive strength of 15 FA CEM is slightly higher than that of 15 WMBA CEM (Fig. 9 (b)). Apart from the influence of reactivity, the lower strength of 15 WMBA CEM is also related to its higher porosity caused by residual metallic Al in WMBA.
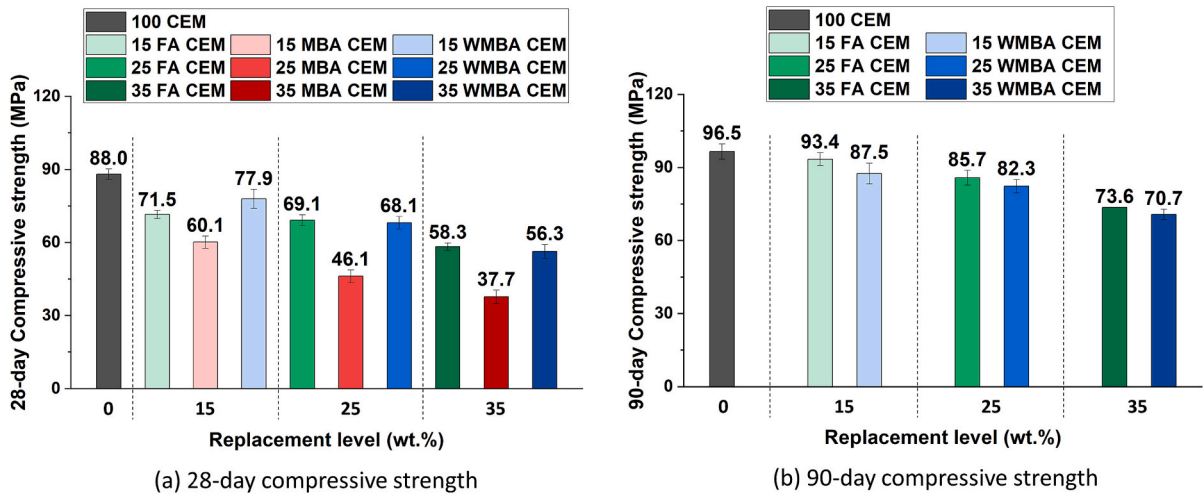
(a) 28-day compressive strength

(b) 90-day compressive strength

Fig. 9. Compressive strength of (a) 28-day cement pastes and (b) 90-day cement pastes.
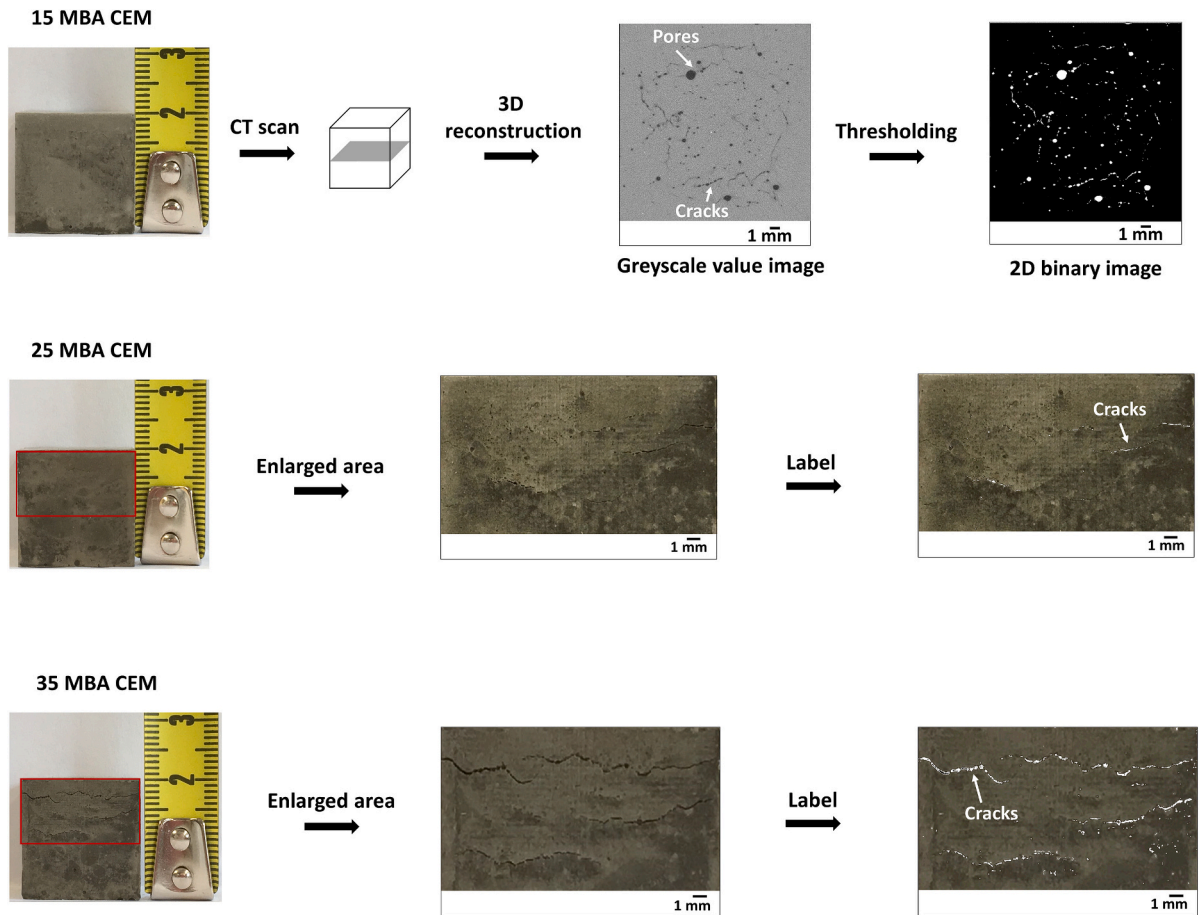

Fig. 10. The cracks and pores of 1-day MBA CEM: Photos of 1-day MBA-CEM samples indicate the cracks and pores on the surface. The greyscale value images and 2D binary images obtained after CT scan and image analysis illustrate the cracks and pores inside 1-day MBA CEM samples. The white areas in the 2D binary images represent the pores and cracks.

Compared with 100 CEM, the compressive strength of WMBA CEM is lower. After being cured for 28 days, the plain cement paste sample had a compressive strength of 88 MPa. The 28-day compressive strength of 15 WMBA CEM was 77.9 MPa, decreasing by 11 % relative to 100 CEM. The 28-day compressive strength of 25 WMBA CEM was 23 % lower than 100 CEM. The differences in the compressive strength between 100 CEM and WMBA CEM became smaller with the prolonging of curing time.

Compared with 100 CEM, the 90-day compressive strength of 15 WMBA CEM and 25 WMBA CEM was 9 % and 15 % lower, respectively.

3.3. Effectiveness of water treatment in eliminating expansive cracks in blended cement pastes prepared with MBA

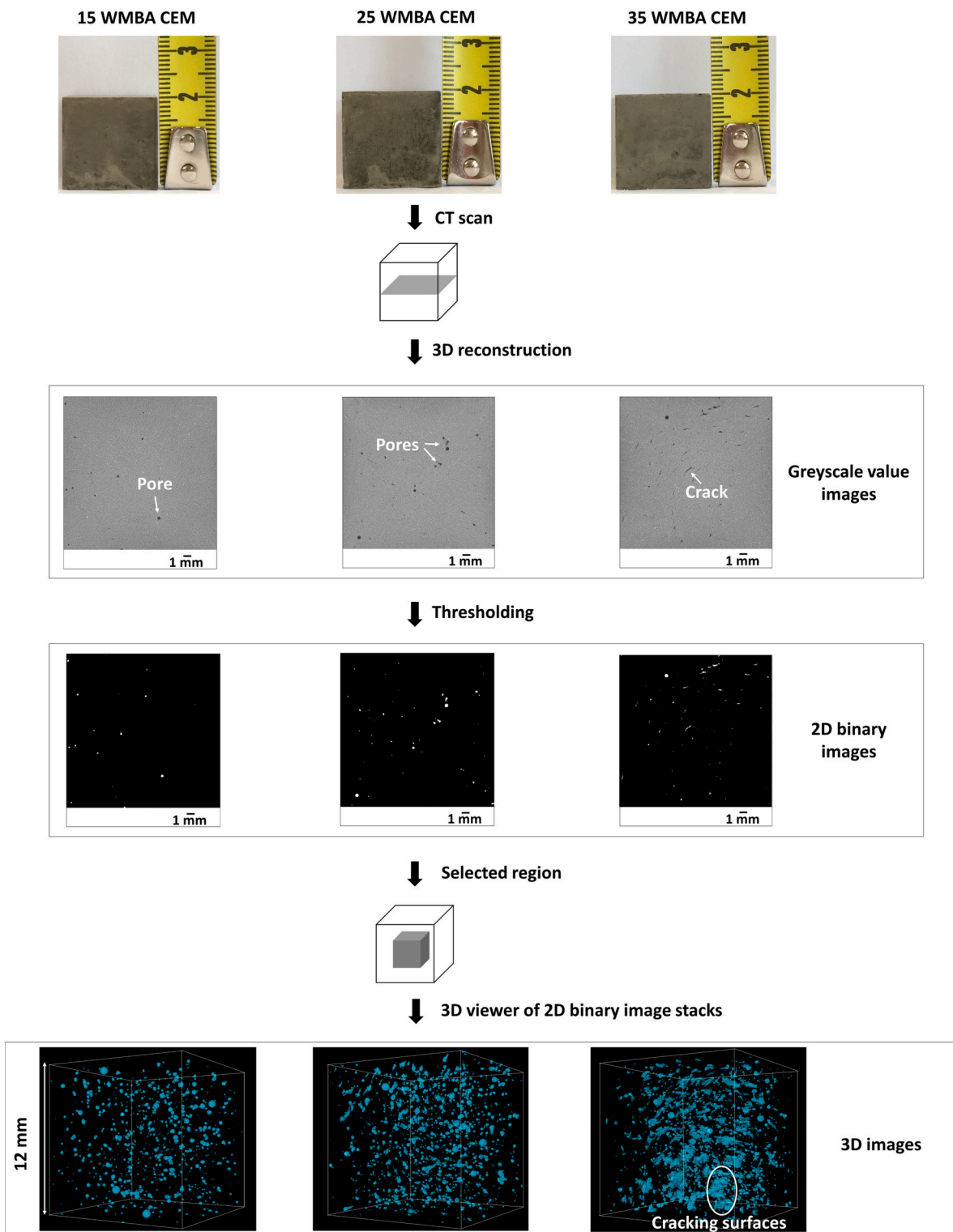As demonstrated in Fig. 10 and Fig. 11, there are more cracks and

Fig. 11. The cracks and pores of 1-day WMBA CEM: Photos of 1-day WMBA CEM samples indicate that there are no cracks or pores on the surface. The greyscale value images, 2D binary images, and 3D images obtained after CT scan and image analysis show the cracks and pores inside 1-day WMBA CEM samples. The white areas in the 2D binary image represent the pores and cracks. The regions colored cyan in 3D images refer to the space occupied by cracks and pores. (For interpretation of the references to color in this figure legend, the reader is referred to the web version of this article.)

pores in MBA CEM than in WMBA CEM due to the higher metallic Al content in MBA. The volume of cracks and pores in blended cement pastes increased with the addition of MBA (see Fig. 10). Although cracks were not found on the surface of 15 MBA CEM, cracks inside cement paste samples can be observed clearly in the 2D binary image obtained after CT scan and image analysis. Cracks can be observed on the surface

of 25 MBA CEM and 35 MBA CEM. Therefore, MBA with 0.13 wt% metallic Al is not suitable to be directly used as SCM in blended cement pastes. In comparison, at the same replacement level (15 wt%, 25 wt%, and 35 wt%), cracks were not observed on the surface of WMBA CEM (Fig. 11).

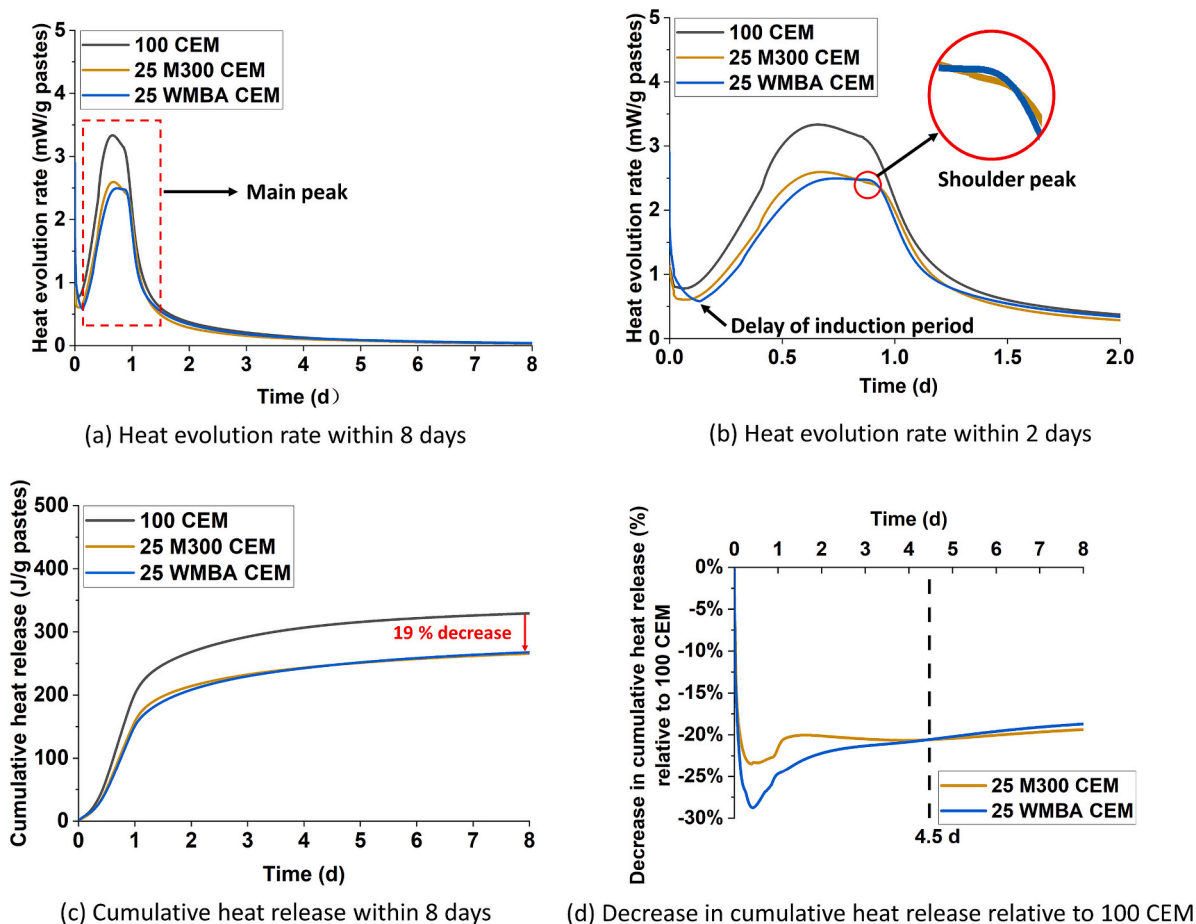As illustrated in the 2D binary images and the 3D images, the volume

(a) Heat evolution rate within 8 days

(b) Heat evolution rate within 2 days

(c) Cumulative heat release within 8 days

(d) Decrease in cumulative heat release relative to 100 CEM

Fig. 12. (a) and (b) Heat release per gram of paste for 100 CEM, 25 M300 CEM, and 25 WMBA CEM. (c) Cumulative heat release per gram of pastes for 100 CEM, 25 M300 CEM, and 25 WMBA CEM. (d) Decrease in cumulative heat release of 25 M300 CEM and 25 WMBA CEM relative to 100 CEM.

occupied by air voids inside WMBA CEM increased with the incorporation of WMBA, from 15 to 35 wt% WMBA. There are no cracks within 15 WMBA CEM and 25 WMBA CEM. Cracks were observed in the 2D binary image of 35 WMBA CEM, and cracking surfaces were found inside 35 WMBA CEM on its 3D image. Considering the adverse effects of metallic Al on strength development, for WMBA with metallic Al content of 0.02 wt%, its replacement for PC may not exceed 25 wt% to avoid cracking of blended cement pastes. The paste sample of 25 WMBA CEM was used in the microstructure analysis to study the reaction of WMBA in blended cement pastes, as will be discussed in the following sections.

3.4. Formation and analysis of the microstructure of cement pastes

As discussed above, after water treatment of MBA, its dosage in blended cement pastes can reach up to 25 wt%. The compressive strength of 25 WMBA CEM is similar to that of 25 FA CEM. In this section, the paste sample of 25 WMBA CEM is analyzed to investigate the role of *water-treated MBA* in the formation of cement paste microstructure. For comparison purposes, the microstructure formation of plain cement paste (100 CEM) and Portland cement paste blended with 25 wt% inert micronized sand (25 M300 CEM) is also studied.

3.4.1. Effect of WMBA on cement hydration

3.4.1.1. Kinetics of hydration. The heat release of 25 WMBA CEM during the first eight days of reaction was studied by isothermal calorimetry (Fig. 12 (a)). As a reference, the reaction heat of 100 CEM and 25 M300 CEM was also recorded. Fig. 12 (b) shows the heat evolution curves

during the first two days of hydration. The results demonstrate that the substitution of PC with 25 wt% M300 did not retard cement hydration, while cement hydration was delayed by around 2.5 h in 25 WMBA CEM. The retardation effect of MSWI bottom addition on cement hydration was also reported in previous research, especially when the replacement level of MSWI bottom ash was between 20 and 30 wt% [16,17,19–22].

The retardation of cement hydration in 25 WMBA CEM is mainly caused by the Ca^{2+} ions released by MBA during water treatment. After 14 days of water treatment, the Ca^{2+} concentration in the liquid filtered from the 14-day slurry reached 845 mg/L (see Table 5). These Ca^{2+} ions increased the initial Ca^{2+} concentration in Portland cement pastes blended with WMBA, thus hindering the release of Ca^{2+} from the hydration of C_3S. Chen et al. [20] also reported that the retardation effect became more severe when MSWI bottom ash with a higher amount of soluble Ca-bearing substances (such as anhydrite and lime) was used as SCM.

The Zn^{2+} ions and organics released due to the water treatment of MBA may also influence cement hydration in 25 WMBA CEM. The $CaZn_2(OH)_6 \cdot 2H_2O$ formed in the presence of zinc ions could inhibit cement hydration at an early age by depositing on the surface of C_3S grains [43–45]. Additionally, the formation of metal hydroxides would reduce the pH in the blended cement system, leading to a retardation in the precipitation of portlandite [45]. A delay in the formation of portlandite would decrease the rate of C_3S hydration. Since MBA contains organics, the adsorption of organics onto the calcium hydroxide nuclei or the initial hydration products of tricalcium aluminate (C_3A) could both impede cement hydration [46].

In the heat evolution curve (in Fig. 12 (b)), the main peak, which came after the induction period, is assigned to cement hydration [47].
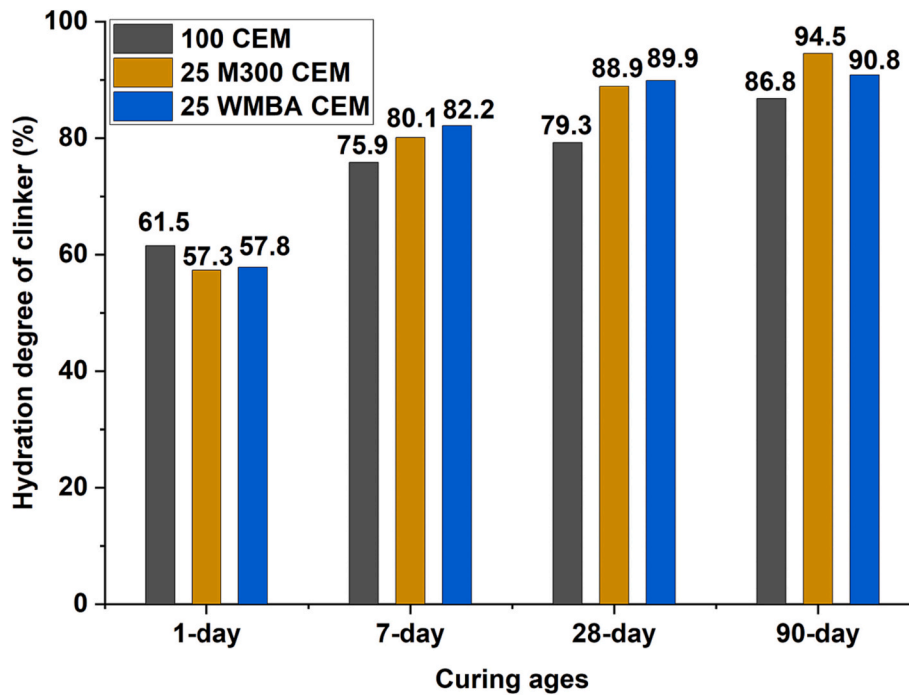
Fig. 13. Hydration degree of clinker in cement pastes, determined according to the QXRD results.

The replacement of PC with WMBA reduced the intensity of this peak. The intensity of the main peak of 25 WMBA CEM is lower than the main peak of 25 M300 CEM. The reason for the lower peak intensity in 25 WMBA CEM is that the incorporation of WMBA in blended cement impeded cement hydration in the initial stage. The shoulder peak observed at around 0.9 day in the deceleration period can be attributed to the heat released during ettringite formation [47]. The shoulder peak of 25 WMBA CEM exhibits a slightly higher intensity than that of 25 M300 CEM (Fig. 12 (b)), suggesting that more ettringite was formed in 1-day 25 WMBA CEM. This deduction was confirmed by the QXRD analysis results (see Fig. 15).

The cumulative heat released by 100 CEM, 25 WMBA CEM, and 25 M300 CEM during the first eight days of reaction is shown in Fig. 12 (c). The hydration of 100 CEM released more heat than that of 25 WMBA CEM and 25 M300 CEM. After eight days of reaction, the reduction in the cumulative heat release caused by substituting PC with 25 wt% M300 or WMBA was around 19 % (Fig. 12 (c)). The heat generated by 25 WMBA CEM started to exceed 25 M300 CEM after 4.5 days of reaction. As illustrated in Fig. 12 (d), the difference in the cumulative heat between 25 WMBA CEM and 100 CEM was smaller than that between 25 M300 CEM and 100 CEM after 4.5 days of curing. This higher amount of heat release in 25 WMBA CEM is caused by the higher degree of clinker hydration and the reaction of WMBA. More explanations will be provided in the following sections.

3.4.1.2. Hydration degree of clinker. The hydration degree of clinker in 100 CEM, 25 WMBA CEM, and 25 M300 CEM is illustrated in Fig. 13. The degree of clinker hydration at specific curing age (DoH $_{clinker,\ t}$) equals the percentage of clinker that has been reacted relative to the clinker initially added to the system. In the calculation, only the main phases in the clinker, including C_3S, C_2S, C_3A, and C_4AF, are considered. The content of these phases in cement pastes was obtained by QXRD analysis, as presented in Appendix Table 1, Appendix Table 2, and Appendix Table 3. The DoH $_{clinker,\ t}$ was calculated using the following equation:

$$DoH_{clinker,t} = \frac{\sum(C_3S + C_2S + C_3A + C_4AF)_{initial} - \sum(C_3S + C_2S + C_3A + C_4AF)_t}{\sum(C_3S + C_2S + C_3A + C_4AF)_{initial}}$$

According to Fig. 13, after 1 day of curing, the fraction of reacted clinker in 100 CEM is 61.5 %, more than that in 25 WMBA CEM and 25 M300 CEM. However, from 7 days to 90 days, the hydration degree of clinker in 25 WMBA CEM and 25 M300 CEM was higher than that in 100 CEM. The heterogeneous nucleation and dilution effect could be the main physical effects responsible for the enhancement of cement hydration in 25WMBA CEM and 25 M300 CEM [48,49]. The M300 and WMBA particles could provide nucleation sites for the heterogeneous precipitation of hydrates [32,48]. Due to the replacement of PC with M300 and WMBA, the water-to-cement ratio in 25 M300 CEM and 25 WMBA CEM is higher than that in 100 CEM (Table 4), resulting in larger water-to-cement distance in 25 M300 CEM and 25 WMBA CEM [50]. The hydrates in 25 M300 CEM and 25 WMBA CEM could have more space to grow, enhancing the clinker hydration [51].

There is no significant difference between 25 WMBA CEM and 25 M300 CEM in the hydration degree of clinker from 1 day to 28 days. The difference in clinker hydration degree between these two samples is more noticeable at 90 days. In the 90-day samples, the hydration degree of clinker reaches 94.5 % in 25 M300 CEM and 90.8 % in 25 WMBA CEM. The higher hydration degree of clinker in 25 M300 CEM can be attributed to the smaller particle size of M300 (see Fig. 2). Since the particle size of M300 is smaller than MBA, it has a larger surface area and thus can provide more nucleation sites for the precipitation of the reaction products.

3.4.2. Reaction products in hardened cement pastes

The mineralogical composition of 25 WMBA CEM was analyzed with XRD to study the effect of WMBA on reaction product formation in blended cement. 100 CEM and 25 M300 CEM were also characterized and compared with 25 WMBA CEM. As shown in Fig. 14, the XRD patterns of 100 CEM, 25 M300 CEM, and 25 WMBA CEM change slightly from 1 day to 90 days. The differences among 100 CEM, 25 M300 CEM, and 25 WMBA CEM are most evident at 2θ below 20° in the XRD patterns.
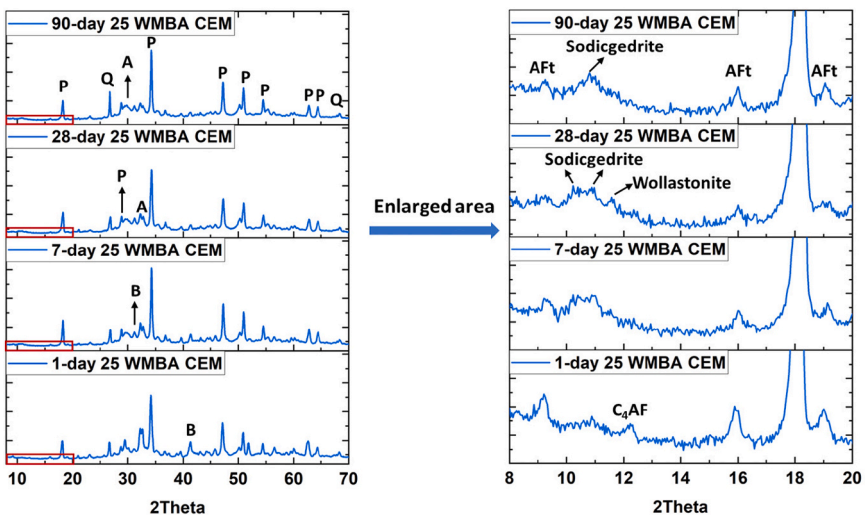
According to the XRD analysis, the reaction products detected in 100 CEM include portlandite ($Ca(OH)_2$, ICSD code 202220), monocarbonate ($Ca_4Al_2(OH)_{12}(CO_3)(H_2O)_5$, ICSD code 59327), monosulfate (AFm) ($Ca_2Al(OH)_6(SO_4)_{0.5}(H_2O)_3$, ICSD code 100138), and ettringite (AFm)
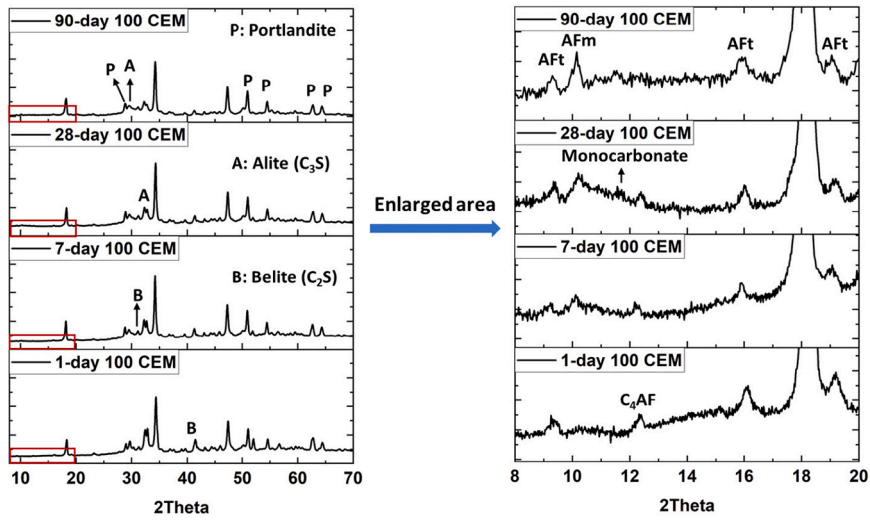
(a) 100 CEM
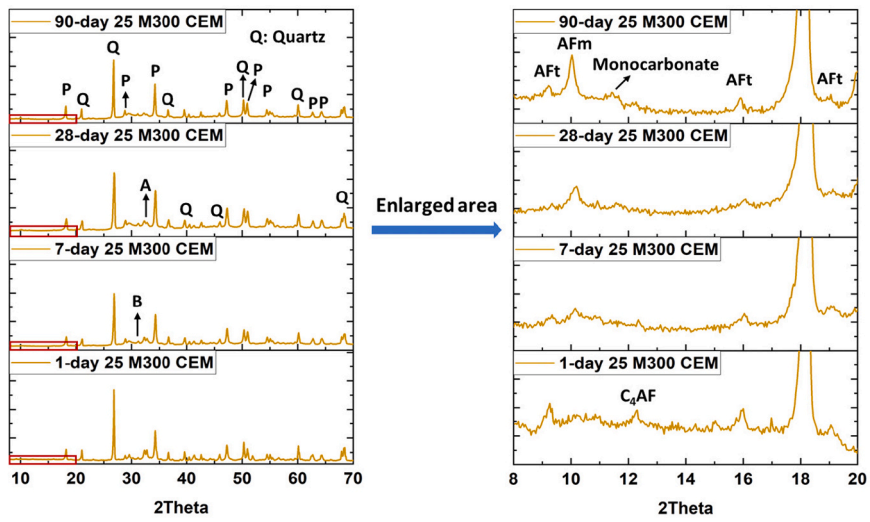
(b) 25 M300 CEM

(c) 25 WMBA CEM

Fig. 14. XRD patterns of 100 CEM, 25 M300 CEM, and 25 WMBA CEM at different curing ages.

(a) Ettringite (AFt)

(b) Monosulfate (AFm)

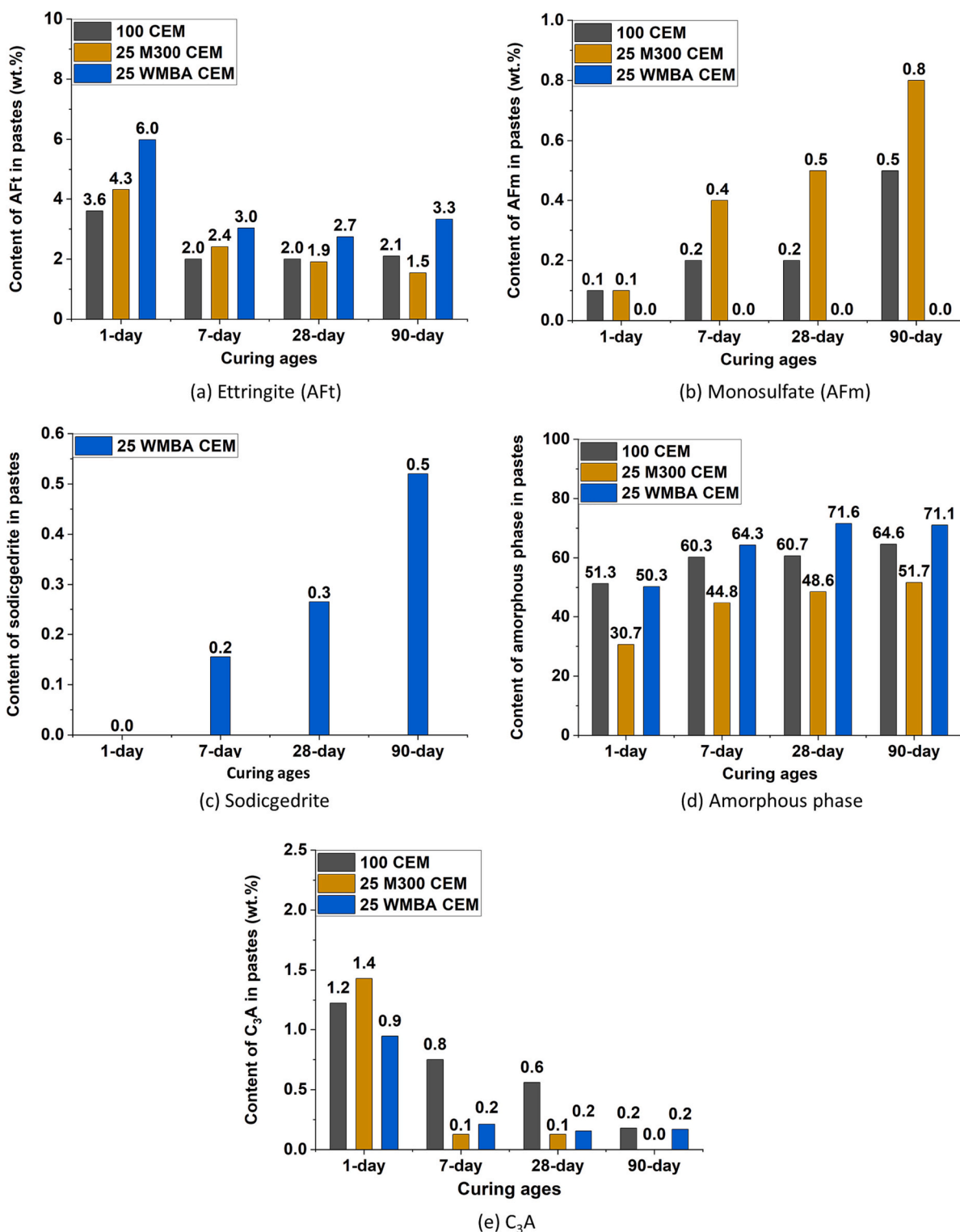(c) Sodicgedrite

(d) Amorphous phase

(e) C₃A

Fig. 15. Content of ettringite, monosulfate, sodicgedrite, amorphous phase, and C3A in 100 CEM, 25 M300 CEM, and 25 WMBA CEM as a function of curing ages, determined by QXRD analysis. This figure was made based on the data presented in Appendix Table 1, Appendix Table 2, and Appendix Table 3.

$(Ca_6Al_2(SO_4)_3(OH)_{12}(H_2O)_{26}$, ICSD code 155395). The reaction products found in 100 CEM were also detected in 25 M300 CEM. However, the types of reaction products in 25 WMBA CEM are slightly different from that of 100 CEM. Monocarbonate and monosulfate (AFm) were not identified in 25 WMBA CEM. Sodicgedirte $(Na_{0.55}(Ca_{0.04}Al_{1.37}Mg_{3.01}Fe_{2.57})(Si_{5.95}Al_{2.05})O_{22}(OH)_2$, ICSD code 34833) is the crystalline reaction product only found in 25 WMBA CEM. The QXRD results of the

reaction products formed in these three cement systems are compared in Fig. 15.

3.4.2.1. Ettringite and monosulfate. At 1 day, the ettringite content in 25 WMBA CEM is higher than in 100 CEM and 25 M300 CEM (Fig. 15 (a)). The higher ettringite content in 25 WMBA CEM is related to the sulfate dissolved from MBA during water treatment. In the solution filtered

Table 7
Elemental concentration of the pore solution of 1-day cement pastes.

1-day paste samples	Concentration in pore solution (mg/L)				Ca/Si molar ratio
	Ca	Si	Al	S	
100 CEM	118	13.1	3.1	336	6.3
25 M300 CEM	310	52	13.1	72	4.2
25 WMBA CEM	134	9.8	2.3	90	9.6

from the 14-day slurry, the concentration of sulfur (S) is 860 mg/L (Table 5). The SO_4^{2-} supplied by MBA increased the sulfate concentrations in the pore solution of 25 WMBA CEM in the initial stage. This increased sulfate concentration would promote the consumption of C_3A, resulting in the formation of a higher amount of ettringite. As illustrated in Fig. 15 (e), the C_3A remained in 1-day 25 WMBA CEM is 0.9 wt%, less than that in 1-day 25 M300 CEM (1.4 wt%).

Fig. 15 (a) shows that the ettringite content in 100 CEM, 25 M300 CEM, and 25 WMBA CEM decreases by around 50 % from 1 day to 7 days. Ettringite usually converts to monosulfate with the decrease of the sulfate content in the pore solution after the consumption of calcium sulfate [52]. The ettringite content decreased, while the monosulfate content increased with the prolonging of curing ages (Fig. 15). However, the reduction in the ettringite content is much higher than the increase in the monosulfate content. One possible explanation is that most of the monosulfate converted from ettringite was poorly crystalline and did not exhibit sharp diffraction peaks in the XRD measurements [53].

It is worth noting that, unlike 25 M300 CEM, the peaks of monosulfate were not found in the XRD patterns of 25 WMBA CEM (Fig. 14). The lower monosulfate content in 25 WMBA CEM can be attributed to the higher sulfate concentration in the pore solution of 1-day 25 WMBA CEM (see Table 7). Since WMBA contains sulfur, sulfate could be released by WMBA in later stages, leading to a higher sulfate concentration in 25 WMBA CEM than in 25 M300 CEM. Thus, the conversion of ettringite to monosulfate was more difficult in 25 WMBA CEM.

From 7 days to 90 days, the ettringite content in 100 CEM, 25 M300 CEM, and 25 WMBA CEM only changed slightly. The majority of the ettringite present in the 7-day samples did not convert to monosulfate. There are two possible reasons for this phenomenon. First, the C_3A

content in PC is limited (around 5 wt%). After 7 days of hydration, only traces of C_3A (< 1 wt%) remained in plain cement paste and blended cement pastes, which is unfavorable to the conversion of ettringite to monosulfate. Second, the calcite present in PC and WMBA may prevent ettringite from reacting with C_3A to form monosulfate. In the presence of carbonate, the crystallization of monocarbonate was favored over monosulfate, as the monocarbonate is more stable at room temperature [54]. Monocarbonate was found in 100 CEM and 25 M300 CEM after 28 days of curing, as illustrated in Appendix Table 1 and Appendix Table 2.

3.4.2.2. Sodicgedrite. After 7 days of reaction, the peaks of sodicgedrite, the magnesium sodium iron aluminate silicate hydroxide, appeared in the XRD patterns of 25 WMBA CEM (Fig. 14 (c)). The peak intensity of this crystalline phase increased with the progress of hydration. The QXRD results show that the content of sodicgedrite increased from 7 days to 90 days (Fig. 15 (c)). Sodicgedrite is not the reaction product of Portland cement hydration. Therefore, sodicgedrite can be the reaction product of WMBA and portlandite, which will be discussed in detail in Section 3.4.3.

3.4.2.3. Amorphous phase. The amorphous phase content in 100 CEM, 25 M300 CEM, and 25 WMBA CEM increased from 1 day to 90 days, which is mainly due to the hydration of clinker. While M300 is unreactive in blended cement, WMBA can contribute to the formation of the amorphous phase from the first day of hydration. The degree of clinker hydration in 1-day 25 WMBA CEM is roughly equivalent to that in 1-day 25 M300 CEM (Fig. 13). In this case, the portlandite content and the Ca^{2+} concentration in 1-day 25 WMBA CEM and 1-day 25 M300 CEM should be within the same range. However, the portlandite content in 25 WMBA CEM is lower than in 25 M300 CEM (Fig. 16). The concentrations of Ca, Al, and Si in the pore solution of 1-day 25 WMBA CEM are much lower than that in 1-day 25 M300 CEM (Table 7). The possible reason could be that the reaction of WMBA consumed portlandite. The reaction product of WMBA may have amorphous structure, such as calcium silicate hydrate (C-S-H), because new crystalline phases were not identified in 1-day 25 WMBA CEM.

There is a drop in the content of portlandite determined by TGA in 25 WMBA CEM (Fig. 16) from 7 days to 28 days. From 7 days to 28 days, the
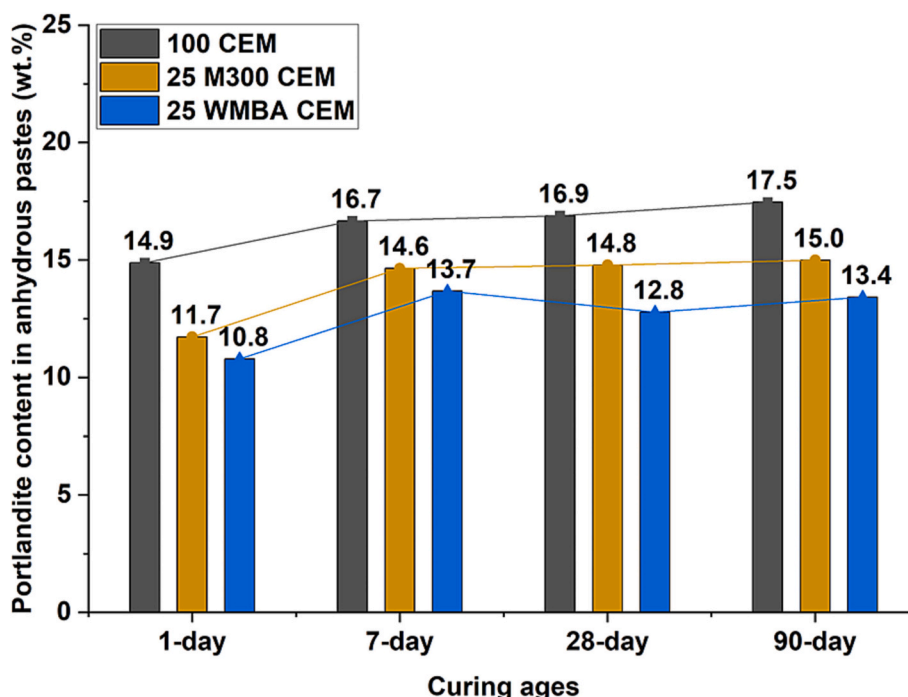

Fig. 16. Portlandite content in anhydrous paste samples determined by TGA.

(a) 90-day 100 CEM (1000 ×)

(b) 90-day 100 CEM (4000 ×)

(c) 90-day 25 M300 CEM (1000 ×)

(d) 90-day 25 M300 CEM (4000 ×)

(e) 90-day 25 WMBA CEM (1000 ×)

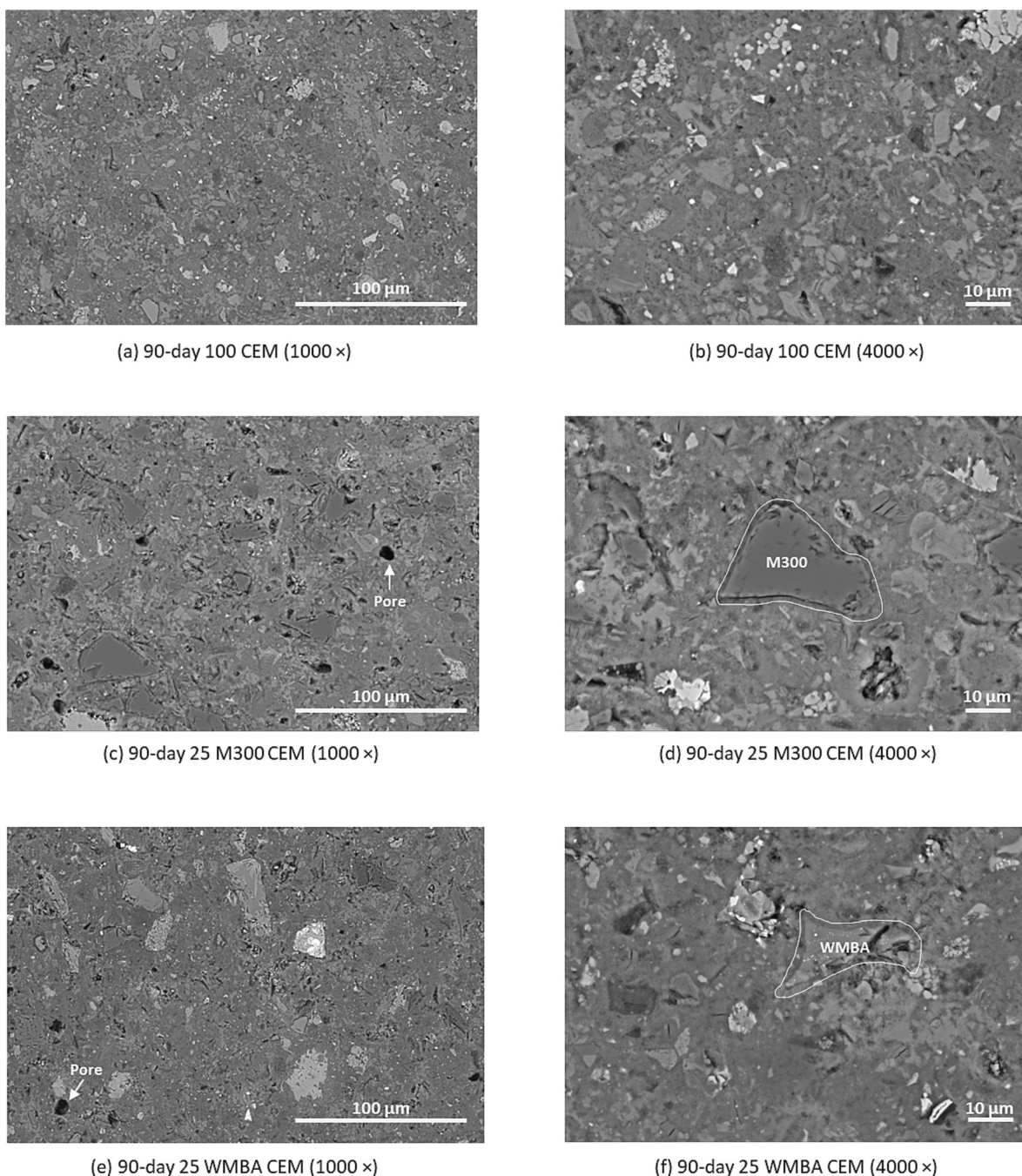(f) 90-day 25 WMBA CEM (4000 ×)

Fig. 17. SEM-BSE images of 100 CEM, 25 M300 CEM, and 25 WMBA CEM paste samples at 90 days. The magnifications are 1000 (left images) and 4000 (right images).

amount of clinker hydrated in 25 WMBA CEM was less than that in 25 M300 CEM (see Fig. 13). In contrast, the content of the amorphous phase in 25 WMBA CEM increased by 7.3 wt%, almost doubling that in 25 M300 CEM (3.8 wt%) (Fig. 15 (d)). For these reasons, some of the portlandite produced after clinker hydration in 25 WMBA CEM should be consumed by WMBA, and the reaction product was the amorphous phase.

3.4.3. Morphology of hardened cement pastes

The morphology of 25 WMBA CEM was observed under SEM to investigate the influence of WMBA on the microstructural development of cement pastes. For comparison purposes, the morphology of 100 CEM and 25 M300 CEM was also studied. Fig. 17 shows the SEM-BSE images

of the 90-day hardened paste samples of 100 CEM, 25 M300 CEM, and 25 WMBA CEM. Since the pores were filled with epoxy during sample preparation, they were identified as the black areas of the SEM-BSE images. Compared with the Portland cement pastes blended with WMBA or M300, the plain cement pastes exhibited a denser microstructure. At the magnification of 1000, more pores were found in 25 WMBA CEM and 25 M300 CEM than in 100 CEM (see Fig. 17 (a), (c), and (e)).

The area surrounding WMBA and M300 particles was examined under high magnification (4000). As shown in Fig. 17 (d) and (f), the WMBA particles and M300 particles both have angular shapes. Unlike the intact M300 particles, cracks were found within the WMBA particles. The grey levels of different regions within a single WMBA particle can
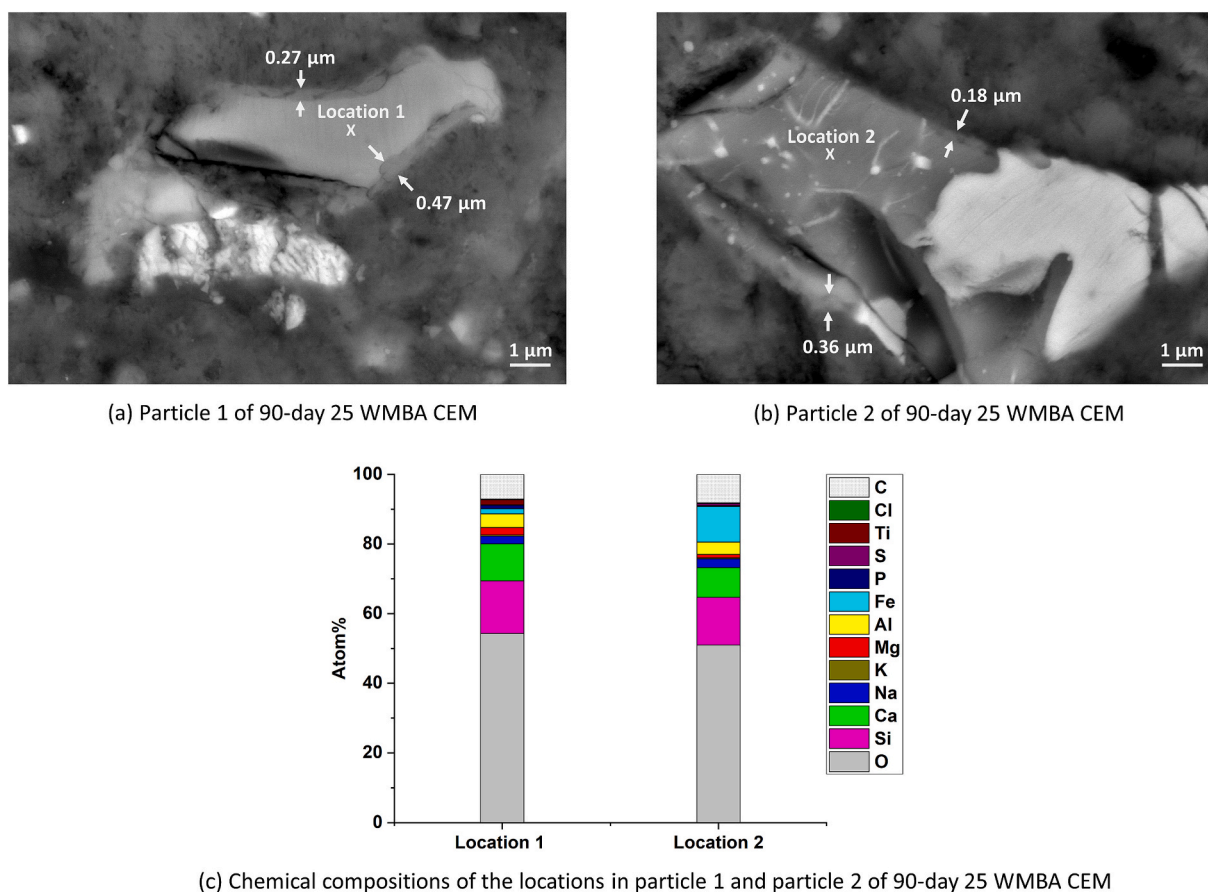
(a) Particle 1 of 90-day 25 WMBA CEM

(b) Particle 2 of 90-day 25 WMBA CEM

(c) Chemical compositions of the locations in particle 1 and particle 2 of 90-day 25 WMBA CEM

Fig. 18. (a) and (b) SEM-BSE images of the partially reacted WMBA particles in 90-day 25 WMBA CEM. (c) SEM-EDS spot analysis results of the locations labeled in particle 1 and particle 2.

differ because of the heterogeneity in chemical compositions. The M300 and WMBA particles labeled in the BSE images were recognized by SEM-EDS spot analysis. The BSE images of 25 M300 CEM and 25 WMBA CEM indicate that a dense microstructure was formed around the M300 and WMBA particles.

Fig. 18 (a) and (b) demonstrate two typical examples of partially reacted WMBA particles in 90-day 25 WMBA CEM. Layers of reaction products were deposited on the surface of these two particles (particle 1 and particle 2). In the SEM-BSE images, the reaction products formed in situ from WMBA have a thickness below 0.5 μm and are brighter in color than the gel formed between unreacted particles. According to the SEM-EDS spot analysis (see Fig. 18 (c)), the elements detected at location 1 of particle 1 and location 2 of particle 2 are mainly Na, Ca, Al, Mg, Fe, Si, and O. These elements are also the constituents of sodicgedrite $(Na_{0.55}(Ca_{0.04}Al_{1.37}Mg_{3.01}Fe_{2.57})(Si_{5.95}Al_{2.05})O_{22}(OH)_2)$. It is possible that the in-situ reaction product of WMBA is sodicgedrite.

The glass particles are the primary resources of the reactive phase in MBA [10]. Given that the mineralogical composition of WMBA is almost the same as that of MBA (see Section 3.1.4), the elemental compositions of particle 1 and particle 2 were compared with the chemical composition of the glass particles in MBA. The SEM-EDS spot analysis was performed on the glass particles separated from as-received MSWI bottom ash [10] to determine the composition of the glass in MBA. The measured compositions were projected onto ternary diagrams (Fig. 19). The ternary diagram depicts the ratios of three elements as positions in an equilateral triangle. As shown in Fig. 19, the atomic ratios of the elements detected at location 1 and location 2 are within the same range as that of elements present in the glass particles. It can be deduced that particle 1 and particle 2, which are reactive in 25 WMBA CEM, are WMBA particles consisting of glass. The sodicgedrite detected in 25

WMBA CEM can be the reaction products of portlandite and the glass particles in WMBA.

3.4.4. Chemical composition of C-S-H gel in hardened cement pastes

The chemical composition of the C-S-H gel formed in 25 WMBA CEM was compared with that of 100 CEM and 25 M300 CEM after 90 days of curing. The composition of C-S-H gel was measured at randomly selected locations in the region between unreacted particles, such as the "point 1" shown in Fig. 20. It is worth mentioning that the chemical composition of the reaction products deposited on the surface of WMBA particles (see Fig. 18) was not measured with SEM-EDS spot analysis. This is because the thickness of these in-situ reaction products is much smaller than the radius of interaction volume between the electron beams and gel phases at 15 kV [34].

The Si/Ca and Al/Ca atomic ratios calculated from the analysis results were plotted in Fig. 21 (a)-(c). The scatter plots indicate that the Si/Ca atomic ratio of the C-S-H gel in 100 CEM is between 0.3 and 0.6, while this ratio changes across a wider range (0.3–0.65) in the C-S-H gel of 25 M300 CEM and 25 WMBA CEM. It seems that replacing 25 wt% PC with M300 or WMBA only had little effect on the Si/Ca atomic ratio of the C-S-H gel. However, in addition to C-S-H gel, the composition information collected at a single location in the SEM-EDS spot analysis may also include signals from other phases, such as ettringite and portlandite. When an electron beam strikes the specimen, the interaction volume may contain two or more phases [33]. It is necessary to separate the signals of C-S-H gel from those of the other phases so as to compare the composition of the gel phases formed in 100 CEM, 25 M300 CEM, and 25 WMBA CEM.

According to the method proposed by Scrivener et al. [33], the Si/Ca and Al/Ca atomic ratios in the C-S-H gel can be estimated by taking the
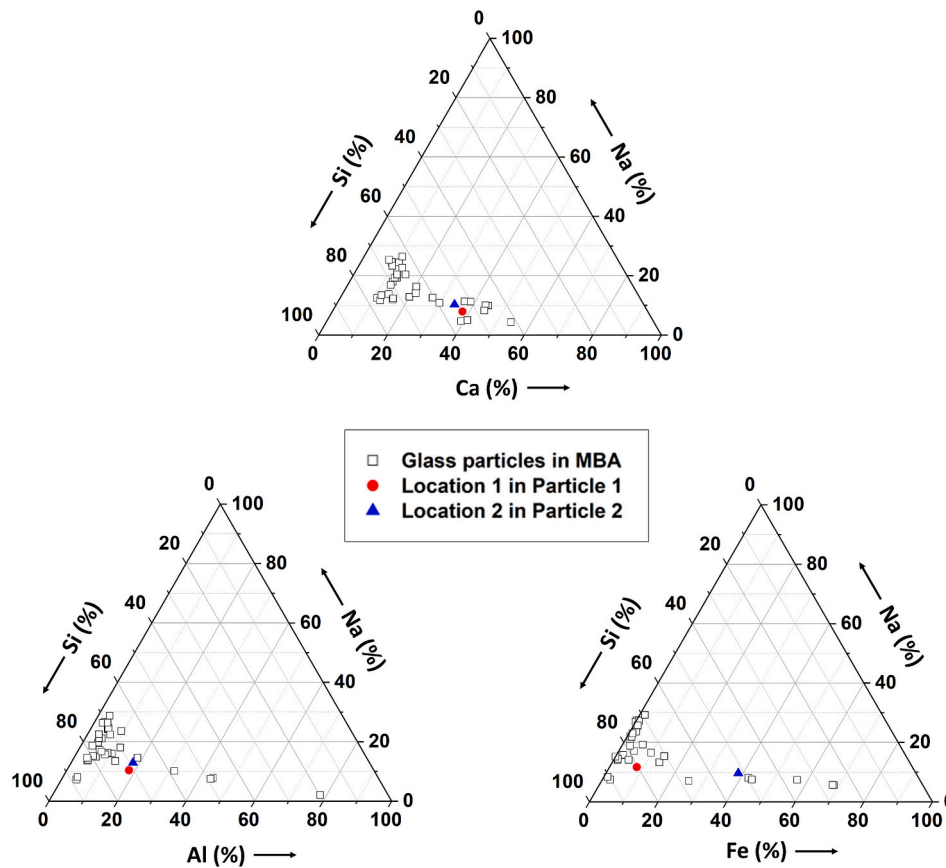
Fig. 19. Comparison between the chemical compositions (atom %) of the glass particles in MBA and the chemical compositions measured at location 1 and location 2 (shown in Fig. 18 (a) and (b)) in 90-day 25 WMBA CEM. The ternary diagrams are plotted according to the atomic percentages of the elements.
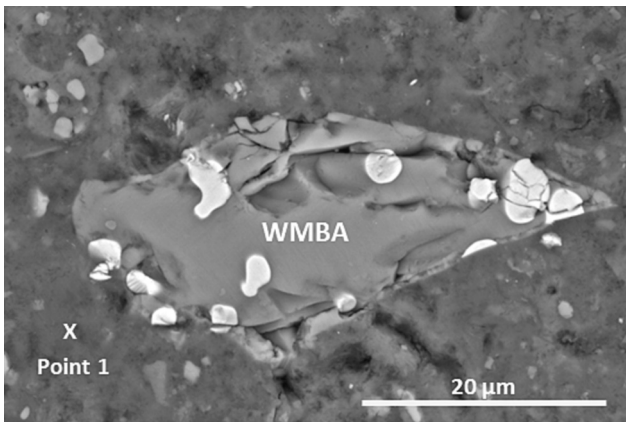

Fig. 20. An example of the location selected for the measurement of C-S-H gel composition in SEM-EDS spot analysis. The sample is 90-day 25 WMBA CEM, and the magnification is 8000.

value at the right edge of the cloud of measured C-S-H compositions in the scatter plots. The point at the right edge is the "least-intermixed point", and its value is very close to the atomic ratio of C-S-H gel. The value represented by the point at the right edge is determined by fitting the dataset of measured composition with Gaussian distribution [34]. Fig. 21 (d)-(f) illustrate the distribution plots of the dataset of the measured Si/Ca and Al/Ca atomic ratios plotted in Fig. 21 (a)-(c). The mean value (μ) of the fitted distribution is taken as the Al/Ca atomic ratio for the C-S-H gel. The Si/Ca atomic ratio of the C-S-H gel is taken to be $\mu + 2\sigma$, where σ represents the standard deviation of the fitted

distribution. The locations of fitted compositions are also labeled in the scattering plots (Fig. 21 (a)-(c)).

The Si/Ca and Al/Ca atomic ratios represented by the edge points of 100 CEM, 25 M300 CEM, and 25 WMBA CEM were summarized in Fig. 22. The Al/Si and Ca/Si atomic ratios were also calculated from the atomic ratios of Si/Ca and Al/Ca. Fig. 22 shows that the Al/Si atomic ratio is almost the same in the C-S-H gel of 100 CEM, 25 M300 CEM, and 25 WMBA CEM. The Ca/Si atomic ratio of the C-S-H gel in 25 WMBA CEM and 25 M300 CEM are nearly equal. Both are lower than the Ca/Si atomic ratio of the C-S-H gel in 100 CEM.

The low Ca/Si atomic ratio of the C-S-H gel in 25 M300 CEM can be attributed to the low Ca/Si molar ratio in the pore solution. Blending PC with M300 reduced the Ca/Si molar ratio in the pore solution. As shown in Table 7, the Ca/Si molar ratio in the pore solution of 1-day 25 M300 CEM is 4.2, lower than that in the pore solution of 1-day 100 CEM (6.3). The Ca/Si molar ratio in the pore solution of Portland cement paste decreased with the prolonging of curing time [55]. Given that the addition of M300 enhanced cement hydration, the decrease of the Ca/Si molar ratio in the pore solution of 25 M300 CEM would be faster than that in the pore solution of 100 CEM. From 1 day to 90 days, the Ca/Si molar ratio in the pore solution of 25 M300 CEM remained lower than that in the pore solution of 100 CEM, resulting in a lower Ca/Si atomic ratio of the C-S-H gel.

In the case of 25 WMBA CEM, the low Ca/Si atomic ratio of the C-S-H gel is mainly caused by the reaction of WMBA. There are three possible explanations:

- First, like the situation in 25 M300 CEM, cement hydration was also accelerated in 25 WMBA CEM due to the heterogeneous nucleation and dilution effect. The Ca/Si molar ratio would decrease faster than that in the pore solution of Portland cement. Besides, as discussed in
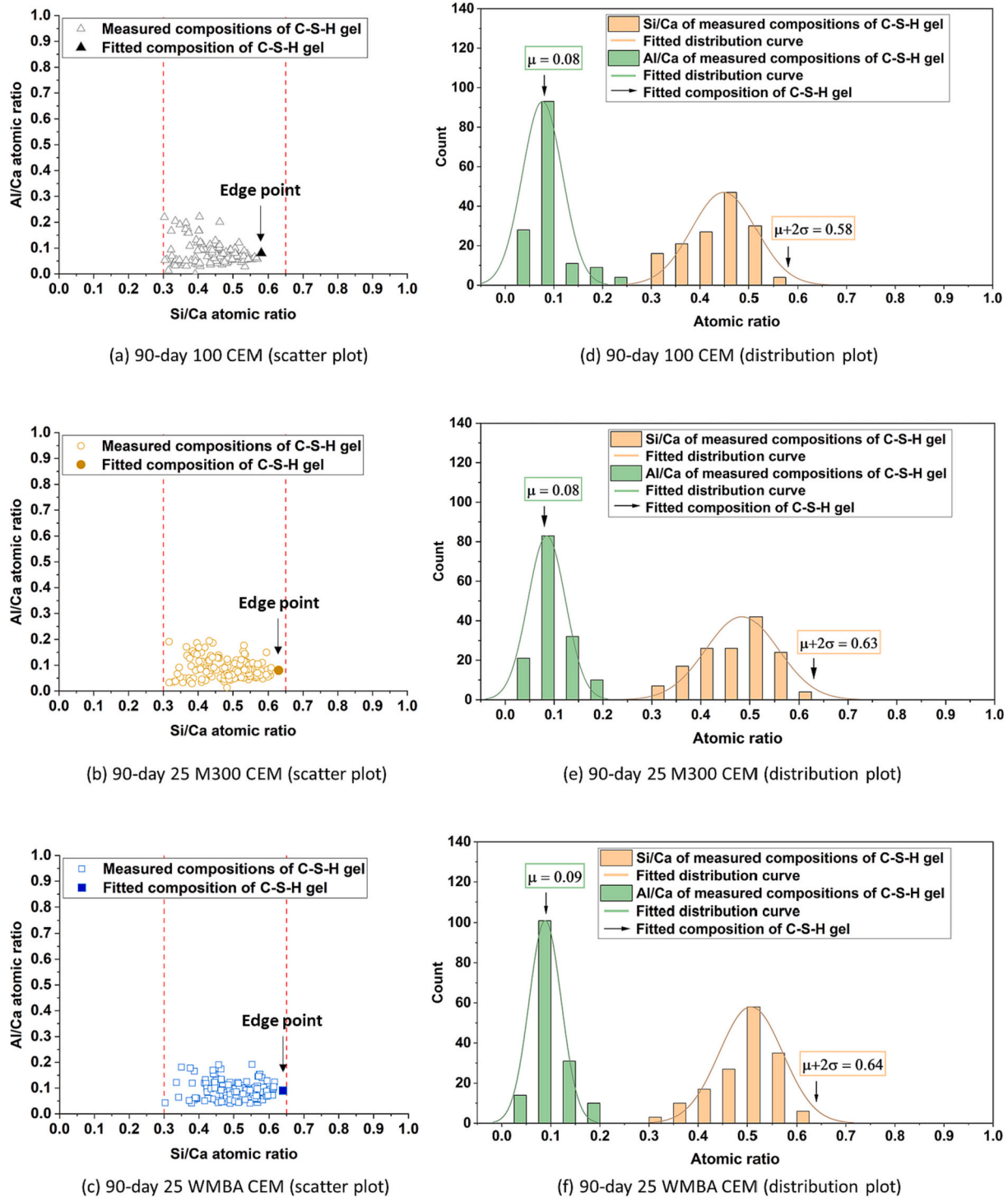
Fig. 21. (a)-(c) The 2D scatter plot of the SEM-EDS analysis results of the C-S-H gel in 100 CEM, 25 M300 CEM, and 25 WMBA CEM at 90 days. (d)-(e) The distribution plot of the SEM-EDS analysis results shown in (a)-(c). The distribution of the data is fitted with a Gaussian curve. The mean (μ) and the standard deviation of the fitted distribution (σ) are used to find the atomic ratio of the elements in C-S-H: Al/Ca (at μ), Si/Ca (at $\mu + 2\sigma$). The points representing fitted compositions are referred to as the "edge points".

Section 3.4.2, the reaction of WMBA in 25 WMBA CEM consumed portlandite. The Ca/Si molar ratio in the pore solution may also decrease after some Ca^{2+} ions were consumed by the reaction of WMBA, resulting in a low Ca/Si atomic ratio of the C-S-H gel.

• Second, the Ca/Si atomic ratio of the C-S-H gel could be lower after incorporating the Si dissolved from WMBA. The mineralogical composition of MBA only slightly changed after water treatment (see Section 3.1). Like MBA, the amorphous phase of WMBA also has

much more Si than Ca [10]. The dissolution of WMBA mainly provided Si to the formation of C-S-H gel, which would increase the Si content in the gel.

• Third, the pozzolanic reaction of WMBA may produce C-S-H gel with a low Ca/Si atomic ratio. Since the chemical compositions of the amorphous phase in WMBA and Class F coal fly ash are within the same range [10], the pozzolanic reaction products of WMBA and Class F coal fly ash could be similar. According to Bentz et al. [56],
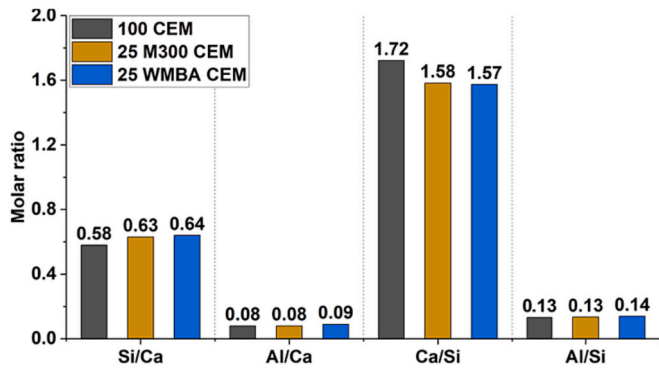
Fig. 22. Comparison of atomic ratios of fitted compositions (at edge points) of the C-S-H in 100 CEM, 25 M300 CEM, and 25 WMBA CEM at 90 days.

the pozzolanic reaction products of coal fly ash can be calcium silicate hydrate (C$_{1.1}$SH$_{3.9}$) and strätlingite (C$_2$ASH$_8$). It is possible that in 25 WMBA CEM, the C$_{1.1}$SH$_{3.9}$ also formed after the pozzolanic reaction of WMBA. When C-S-H gel with a low Ca/Si atomic ratio was mixed with the C-S-H gel formed after cement hydration, the overall Ca/Si atomic ratio of the C-S-H gel in 25 WMBA CEM was decreased.

Based on what has been discussed above, it is difficult to distinguish the C-S-H gel formed in 25 WMBA CEM and 25 M300 CEM by comparing the Ca/Si or the Al/Si atomic ratio. However, the alkali contents are different in the C-S-H gel of 25 WMBA CEM and 25 M300 CEM. As shown in Fig. 23, blending PC with M300 did not change the (Na + K)/Si atomic ratio of the C-S-H gel. Comparatively, more alkali ions were incorporated in the C-S-H gel formed in 25 WMBA CEM. These extra alkali ions were released by WMBA (Fig. 18(c)).

3.4.5. Porosity of hardened cement pastes

The porosity of the 90-day 25 WMBA CEM was measured by the nitrogen adsorption test. The test result was compared with that of 90-day 100 CEM and 25 M300 CEM (see Fig. 24). The nitrogen adsorption test mainly measured the volumes of the capillary pores ranging from 2 to 500 nm [57]. The gel pores with their characteristic size of 1.5 to 2 nm [58] cannot be measured with this technique.

As illustrated in Fig. 24 (a), the total pore volume in 90-day hardened pastes increased in the following order: 100 CEM < 25 WMBA CEM < 25 M300 CEM. The differential curve of 90-day 100 CEM displays a unimodal distribution (Fig. 24 (b)). The corresponding critical pore width is 20 nm. In the differential curve of 90-day 25 WMBA, the main peak was observed at 22.5 nm, which shifted slightly to the larger pore width relative to the peak of 90-day 100 CEM. Unlike 90-day 100 CEM and 25 WMBA CEM, the differential curve of 90-day 25 M300 CEM shows a bimodal distribution. The first peak was found at the same pore
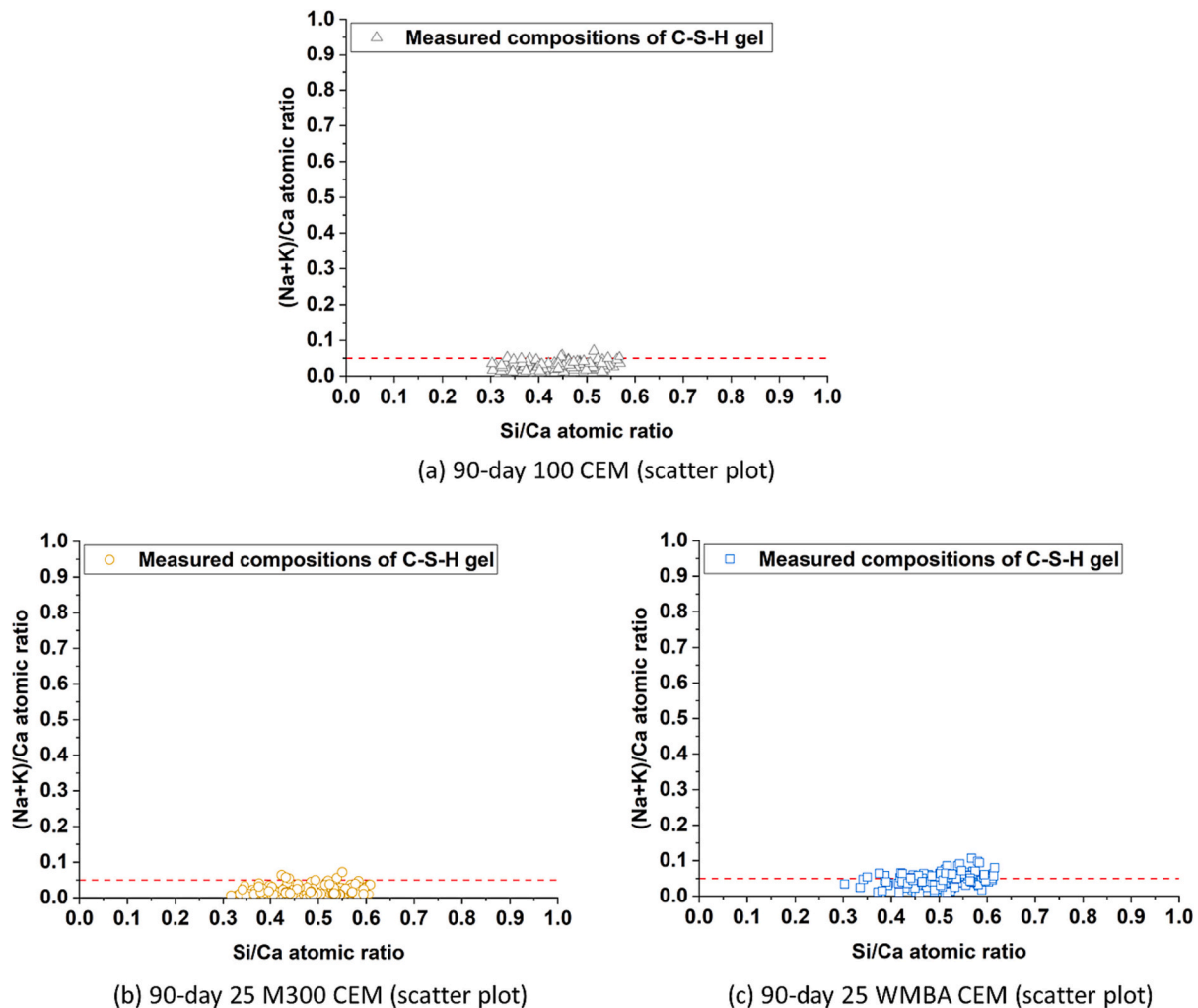

Fig. 23. (a)-(c) The 2D scatter plot of the SEM-EDS analysis results of the C-S-H gel in 100 CEM, 25 M300 CEM, and 25 WMBA CEM at 90 days. For comparison purposes, the axis scale settings are the same as those of the scatter plots shown in Fig. 21.
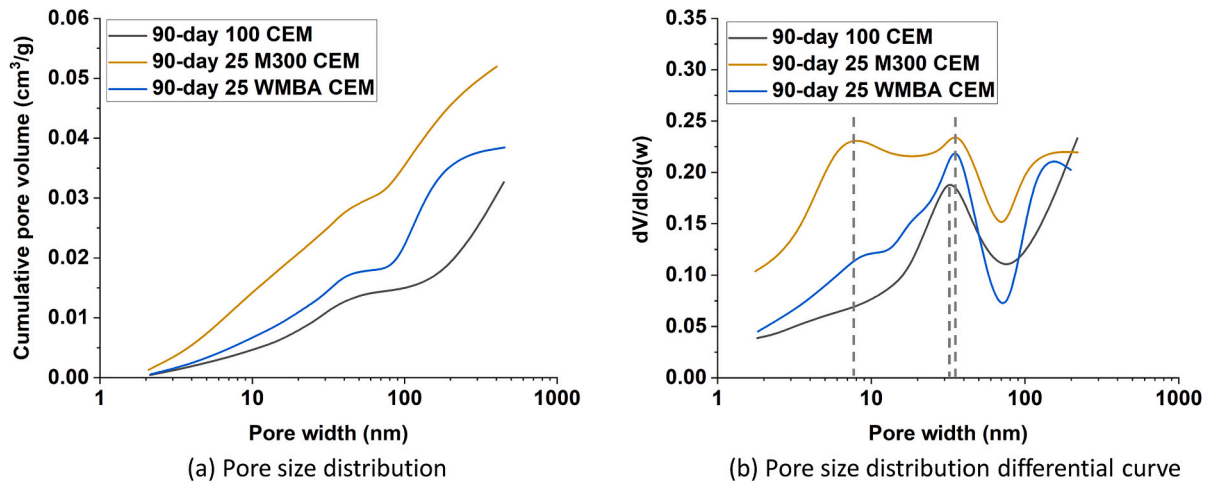
(a) Pore size distribution   (b) Pore size distribution differential curve

Fig. 24. Pore size distribution of 100 CEM, 25 M300 CEM, and 25 WMBA CEM at 90 days, determined using the nitrogen adsorption method.
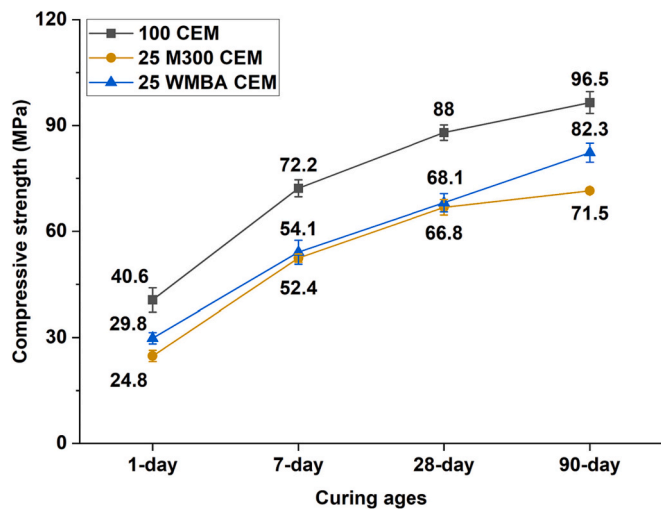

Fig. 25. Compressive strength of cement pastes as a function of curing ages.

width as the main peak of 90-day 25 WMBA CEM. The second peak of 90-day 25 M300 CEM appeared at the pore width of 8 nm.

Compared with 100 CEM, less PC was used for the preparation of 25 WMBA CEM and 25 M300 CEM, reducing the quantities of reaction products. As a result, the porosity of 25 WMBA CEM and 25 M300 CEM is higher. When comparing 90-day 25 WMBA CEM and 25 M300 CEM, the porosity of 25 WMBA CEM is observed to be lower, which can be explained by the generation of higher amount of reaction products. It is worth noting that the reaction products formed after clinker hydration are fewer in 25 WMBA CEM than in 25 M300 CEM (Fig. 13). The formation of a denser microstructure in 90-day 25 WMBA CEM can be attributed to the reaction products of WMBA particles filling the capillary pores, especially those smaller than 10 nm.

3.5. Strength development of hardened cement pastes

Fig. 25 shows the compressive strength of 25 WMBA CEM at different curing ages. The compressive strength of 100 CEM and 25 M300 CEM was also provided for comparison. Regardless of the curing age, the

compressive strength of 100 CEM is the highest among all these three mixtures. Compared with 100 CEM, the replacement of 25 wt% PC with WMBA reduced the compressive strength by around 15 % at the age of 90 days. The compressive strength of 25 WMBA CEM is higher than that of 25 M300 CEM, which is more evident at 1 day and 90 days.

The 1-day compressive strength of 25 WMBA CEM is 29.8 MPa, which is 5 MPa higher than the strength of 1-day 25 M300 CEM. The higher 1-day compressive strength of 25 WMBA CEM is mainly due to the formation of a larger amount of ettringite. As discussed in Section 3.4.1 and Section 3.4.2, clinker hydration degree in 25 WMBA CEM is almost equal to that in 25 M300 CEM. The SO_4^{2-} dissolved from WMBA particles facilitates ettringite formation. After 1-day curing, the total amount of reaction products in 25 WMBA CEM is more than that in 25 M300 CEM.

At 90 days, the compressive strength of 25 WMBA CEM reaches 82.3 MPa, which is 10.8 MPa larger than that of 25 M300 CEM. A denser microstructure in 90-day 25 WMBA CEM explains its higher compressive strength. The porosity of 90-day 25 WMBA CEM is smaller than that of 25 M300 CEM. Unlike M300, WMBA is reactive, and its reaction products can fill the capillary pores, thereby reducing the volume of capillary pores in 25 WMBA CEM (see Section 3.4.5).

4. Conclusions

In this work, the microstructure formation and strength development of blended cement pastes prepared using MSWI bottom ash (MBA) as supplementary cementitious material were studied. Water treatment of MBA was included in the sample preparation process to improve the compressive strength of MBA blended cement pastes. Compared with plain cement paste (100 CEM), adding water-treated MBA (WMBA) to Portland cement paste affected clinker hydration and changed the reaction products and microstructure of cement pastes. WMBA could participate in the reaction product formation in blended cement pastes and contribute to the strength development. The following are the findings of this work:

- The water treatment of MBA, performed at room temperature during the preparation of blended cement pastes, could reduce the metallic aluminum (Al) content by 85 %, reaching 0.02 wt% in WMBA. Due to water treatment, the replacement level of MBA in blended cement

pastes can reach up to 25 wt% without the formation of cracks caused by hydrogen gas release. The 28-day and 90-day compressive strength of Portland cement pastes blended with WMBA (WMBA CEM) was close to that of Portland cement pastes blended with Class F coal fly ash (FA).

- In the process of water treatment, the dissolution of MBA in water created an alkaline environment to facilitate the corrosion of metallic Al embedded in MBA. The water treatment only slightly changed the mineralogical compositions of MBA by increasing the contents of amorphous phase and calcite.
- Compared with 100 CEM, the incorporation of WMBA delayed cement hydration on the first day, but the hydration of clinker was enhanced at later ages in blended cement pastes prepared with 25 wt% MBA and 75 wt% Portland cement (25 WMBA CEM). After 90 days, the hydration degree of clinker in 25 WMBA CEM was higher than that in 100 CEM. The sulfate dissolved from MBA during water treatment increased the initial sulfate concentration in blended cement and thus promoted the ettringite formation in 1-day 25 WMBA CEM.
- In 25 WMBA CEM, the reaction of WMBA consumed portlandite, and the reaction products of WMBA were sodicgedrite and amorphous phase. The pozzolanic reaction of WMBA may produce C-S-H gel with a lower Ca/Si ratio. The Ca/Si ratio of the C-S-H gel was smaller than that of the C-S-H gel generated in 100 CEM.
- Although the Al/Si and Ca/Si atomic ratios were almost the same in the C-S-H gel formed in 25 WMBA CEM and Portland cement pastes blended with 25 wt% M300 (25 M300 CEM), the C-S-H gel in 25 WMBA CEM incorporated more alkali ions. More reaction products were formed in 25 WMBA CEM than in 25 M300 CEM to fill the capillary pores. The compressive strength of 25 WMBA CEM was higher than 25 M300 CEM.

CRediT authorship contribution statement

Boyu Chen: Conceptualization, Data curation, Formal analysis, Investigation, Methodology, Writing – original draft, Writing – review & editing. **Guang Ye:** Supervision, Writing – review & editing.

Declaration of competing interest

The authors declare that they have no known competing financial interests or personal relationships that could have appeared to influence the work reported in this paper.

Data availability

Data will be made available on request.

Acknowledgments

Appendix A. Appendix

Appendix Table 1
Mineralogical composition of 100CEM at different curing ages, determined by QXRD.

Phases (wt%)	100 CEM			
	1-day	7-day	28-day	90-day
Alite (C_3S)	11	3	2.4	0.9
Belite(C_2S)	10.1	9.7	8.3	5.3
C_3A cubic	0.6	0.5	0.4	0.2
C_3A orthorombic	0.7	0.3	0.1	0
C_4AF	3.3	2.7	2.5	2.4
Calcite	0.2	0.2	0.2	0.5
Mayenite	0.8	0.3	0	0
Bassanite	1.8	2	2	2
Quartz	0.2	0.2	0.2	0.2
Cristobalite	0.5	0.5	0.5	0.5
Arcanite	0.2	0	0	0
Periclase	0.8	0.5	0.5	0.4
Monocarbonate	0	0	2.3	2.6
Portlandite	14.8	17.6	17.7	17.8
Monosulfate (AFm)	0.1	0.2	0.2	0.5
Ettringite (AFt)	3.6	2	2	2.1
Amorphous phase	51.3	60.3	60.7	64.6
Sum	100	100	100	100

Appendix Table 2
Mineralogical composition of 25 M300 CEM at different curing ages, determined by QXRD.

Phases (wt%)	25 M300 CEM			
	1-day	7-day	28-day	90-day
Alite (C_3S)	8	0.6	0	0
Belite(C_2S)	8.9	7.8	4.6	1.8
C_3A orthorombic	1.4	0.1	0.1	0
C_4AF	3.1	1.5	0.9	0.9
Calcite	0.8	0.2	0.2	0.3
Mayenite	1	0.7	0.7	0.7
Bassanite	1.2	1.6	1.1	0.7
Quartz	25.4	23.3	23.3	23.3
Cristobalite	0.5	0.4	0.3	0.3
Arcanite	0	0	0	0
Periclase	0.4	0.5	0.3	0.3
Monocarbonate	0.0	0.0	1.7	1.9
Portlandite	14.2	15.7	15.8	15.8
Monosulfate (AFm)	0.1	0.4	0.5	0.8
Ettringite (AFt)	4.3	2.4	1.9	1.5
Amorphous phase	30.7	44.8	48.6	51.7
Sum	100.0	100.0	100.0	100.0

Appendix Table 3
Mineralogical composition of 25 WMBA CEM at different curing ages, determined by QXRD.

Phases (wt%)	25 WMBA CEM			
	1-day	7-day	28-day	90-day
Alite (C_3S)	7.6	0.5	0	0
Belite(C_2S)	9.1	8.3	4.9	4.4
C_3A cubic	0.3	0	0	0
C_3A orthorombic	0.6	0.2	0.2	0.2
C_4AF	3.4	0	0	0
Calcite	0.4	0.4	0.5	0.2
Mayenite	1.5	0.8	0.3	0
Bassanite	0.4	0.3	0.0	0.0
Quartz	3.0	3.0	3.0	2.9
Cristobalite	0.2	0.2	0.2	0.2
Arcanite	0	0	0	0
Periclase	0.8	0.5	0.3	0.2
Portlandite	11.8	14.4	12.3	13.4
Ettringite (AFt)	6.0	3.0	2.7	3.3
Sodicgedrite	0.0	0.2	0.3	0.5
Magnetite	0.4	0.3	0.2	0.2
Hematite	0.3	0.1	0.1	0.1
Gehlenite	1.1	1.1	1.1	1
Orthopyroxene	0.4	0.1	0	0
Diopside	1	0.9	0.9	0.9
Wollastonite	1.4	1.4	1.4	1.4
Amorphous phase	50.3	64.3	71.6	71.1
Sum	100	100	100	100

References

[1] S. Kaza, L. Yao, P. Bhada-Tata, F. Van Woerden, What a Waste 2.0: A Global Snapshot of Solid Waste Management to 2050, The World Bank, 2018.

[2] S.-Y. Pan, M.A. Du, I.-T. Huang, I.-H. Liu, E.-E. Chang, P.-C. Chiang, Strategies on implementation of waste-to-energy (WTE) supply chain for circular economy system: a review, J. Clean. Prod. 108 (2015) 409–421, https://doi.org/10.1016/j.jclepro.2015.06.124.

[3] A. Tozlu, E. Özahi, A. Abuşoǧlu, Waste to energy technologies for municipal solid waste management in Gaziantep, Renew. Sust. Energ. Rev. 54 (2016) 809–815, https://doi.org/10.1016/J.RSER.2015.10.097.

[4] R. Bunge, Recovery of Metals from Waste Incinerator Bottom Ash. https://vbsa.ch/wp-content/uploads/2016/07/Studie-Bunge-Internetversion.pdf, 2016.

[5] J. Kim, B.H. Nam, B.A. Al Muhit, K.M. Tasneem, J. An, Effect of chemical treatment of MSWI bottom ash for its use in concrete, Mag. Concr. Res. 67 (2015) 179–186, https://doi.org/10.1680/macr.14.00170.

[6] B. Chen, P. Perumal, M. Illikainen, G. Ye, A review on the utilization of municipal solid waste incineration (MSWI) bottom ash as a mineral resource for construction materials, J. Build. Eng. (2023) 106386, https://doi.org/10.1016/j.jobe.2023.106386.

[7] J.M. Chimenos, M. Segarra, M.A. Fernandez, F. Espiell, Characterization of the bottom ash in municipal solid waste incinerator, J. Hazard. Mater. A. 64 (1999) 211–222.

[8] K.L. Lin, D.F. Lin, Hydration characteristics of municipal solid waste incinerator bottom ash slag as a pozzolanic material for use in cement, Cem. Concr. Compos. 28 (2006) 817–823, https://doi.org/10.1016/j.cemconcomp.2006.03.003.

[9] A.M. Joseph, Processed Bottom Ash Based Sustainable Binders for Concrete. http://hdl.handle.net/1854/LU-8694932, 2021.

[10] B. Chen, Y. Zuo, S. Zhang, L.M. de Lima Junior, X. Liang, Y. Chen, M.B. van Zijl, G. Ye, Reactivity and leaching potential of municipal solid waste incineration (MSWI) bottom ash as supplementary cementitious material and precursor for alkali-activated materials, Constr. Build. Mater. 409 (2023) 133890, https://doi.org/10.1016/j.conbuildmat.2023.133890.

[11] N. Saikia, G. Cornelis, G. Mertens, J. Elsen, K. Van Balen, T. Van Gerven, C. Vandecasteele, Assessment of Pb-slag, MSWI bottom ash and boiler and fly ash for using as a fine aggregate in cement mortar, J. Hazard. Mater. 154 (2008) 766–777, https://doi.org/10.1016/j.jhazmat.2007.10.093.

[12] B. Simões, P.R. da Silva, R.V. Silva, Y. Avila, J.A. Forero, Ternary mixes of self-compacting concrete with fly ash and municipal solid waste incinerator bottom ash, Appl. Sci. 11 (2021) 1–17, https://doi.org/10.3390/app11010107.

[13] P. Filipponi, A. Polettini, R. Pomi, P. Sirini, Physical and mechanical properties of cement-based products containing incineration bottom ash, Waste Manag. 23 (2003) 145–156, https://doi.org/10.1016/S0956-053X(02)00041-7.

[14] A.M. Joseph, S. Matthys, N. De Belie, Reactivity of municipal solid waste incineration ashes as a supplementary cementitious material, in: 15th Int. Congr. Chem. Cem., ICCC, 2019.

[15] B. Verbinnen, P. Billen, J. Van Caneghem, C. Vandecasteele, Recycling of MSWI bottom ash: a review of chemical barriers, Engineering Applications and Treatment Technologies, Waste and Biomass Valorization 8 (2017) 1453–1466, https://doi.org/10.1007/s12649-016-9704-0.

[16] P. Tang, M.V.A. Florea, P. Spiesz, H.J.H. Brouwers, Application of thermally activated municipal solid waste incineration (MSWI) bottom ash fines as binder substitute, Cem. Concr. Compos. 70 (2016) 194–205, https://doi.org/10.1016/j.cemconcomp.2016.03.015.

[17] A.M. Joseph, R. Snellings, P. Nielsen, S. Matthys, N. De Belie, Pre-treatment and utilisation of municipal solid waste incineration bottom ashes towards a circular economy, Constr. Build. Mater. 260 (2020) 120485, https://doi.org/10.1016/j.conbuildmat.2020.120485.

[18] L. Bertolini, M. Carsana, D. Cassago, A.Q. Curzio, M. Collepardi, MSWI ashes as mineral additions in concrete, Cem. Concr. Res. 34 (2004) 1899–1906, https://doi.org/10.1016/j.cemconres.2004.02.001.

[19] S. Zhang, Z. Ghouleh, Z. He, L. Hu, Y. Shao, Use of municipal solid waste incineration bottom ash as a supplementary cementitious material in dry-cast concrete, Constr. Build. Mater. 266 (2021), https://doi.org/10.1016/j.conbuildmat.2020.120890.

[20] Z. Chen, E.H. Yang, Early age hydration of blended cement with different size fractions of municipal solid waste incineration bottom ash, Constr. Build. Mater. 156 (2017) 880–890, https://doi.org/10.1016/j.conbuildmat.2017.09.063.

[21] P. Tang, W. Chen, D. Xuan, Y. Zuo, C.S. Poon, Investigation of cementitious properties of different constituents in municipal solid waste incineration bottom ash as supplementary cementitious materials, J. Clean. Prod. 258 (2020), https://doi.org/10.1016/j.jclepro.2020.120675.

[22] E. Loginova, K. Schollbach, M. Proskurnin, H.J.H. Brouwers, Municipal solid waste incineration bottom ash fines: transformation into a minor additional constituent for cements, Resour. Conserv. Recycl. 166 (2021), https://doi.org/10.1016/j.resconrec.2020.105354.

[23] P.K. Mehta, P.J.M. Monteiro, Concrete: microstructure, properties, and materials, McGraw-Hill Education, 2014.

[24] B. Chen, Utilization of Mswi Bottom Ash as a Mineral Resource for Low-Carbon Construction Materials: Quality-Upgrade Treatments, Mix Design Method, and Microstructure Analysis, Delft University of Technology, 2023. https://repository.tudelft.nl/islandora/object/uuid:0793986f-b875-4693-a0f9-568978f2d632.

[25] B. Chen, J. Chen, F.F. de Mendonça Filho, Y. Sun, M.B. van Zijl, O. Copuroglu, G. Ye, Characterization and Mechanical Removal of Metallic Aluminum (Al) Embedded in Weathered Municipal Solid Waste Incineration (MSWI) Bottom Ash for Application as Supplementary Cementitious Material, Waste Manag. (2024).

[26] Z.T. Yao, X.S. Ji, P.K. Sarker, J.H. Tang, L.Q. Ge, M.S. Xia, Y.Q. Xi, A comprehensive review on the applications of coal fly ash, Earth-Science Rev. 141 (2015) 105–121, https://doi.org/10.1016/j.earscirev.2014.11.016.

[27] NEN Connect, NEN-EN 196-1. https://connect.nen.nl/Standard/Detail/219352?compId=10037&collectionId=0, 2016.

[28] G.W. Zack, W.E. Rogers, S.A. Latt, Automatic measurement of sister chromatid exchange frequency, J. Histochem. Cytochem. 25 (1977) 741–753, https://doi.org/10.1177/25.7.70454.

[29] B. Schmid, J. Schindelin, A. Cardona, M. Longair, M. Heisenberg, A high-level 3D visualization API for Java and ImageJ, BMC Bioinformatics. 11 (2010) 274, https://doi.org/10.1186/1471-2105-11-274.

[30] R.S. Barneyback, S. Diamond, Expression and analysis of pore fluids from hardened cement pastes and mortars, Cem. Concr. Res. 11 (1981) 279–285, https://doi.org/10.1016/0008-8846(81)90069-7.

[31] Standard Practice for Measuring Hydration Kinetics of Hydraulic Cementitious Mixtures Using Isothermal Calorimetry. https://www.astm.org/c1679-17.html, 2023.

[32] B. Lothenbach, K. Scrivener, R.D. Hooton, Supplementary cementitious materials, Cem. Concr. Res. 41 (2011) 1244–1256, https://doi.org/10.1016/j.cemconres.2010.12.001.

[33] K. Scrivener, R. Snellings, B. Lothenbach, A Practical Guide to Microstructural Analysis of Cementitious Materials, CRC Press, 2018.

[34] J.E. Rossen, K.L. Scrivener, Optimization of SEM-EDS to determine the C–A–S–H composition in matured cement paste samples, Mater. Charact. 123 (2017) 294–306.

[35] E.P. Barrett, L.G. Joyner, P.P. Halenda, The determination of pore volume and area distributions in porous substances. I. Computations from nitrogen isotherms, J. Am. Chem. Soc. 73 (1951) 373–380.

[36] J. Petrovic, G. Thomas, Reaction of Aluminum with Water to Produce Hydrogen-2010 Update, 2011.

[37] 826 pH mobile / 827 pH lab Manual. https://www.metrohm.com/content/metrohm/en_nl/products/2/8270/28270114.html, 2010.

[38] H.-T. Teng, T.-Y. Lee, Y.-K. Chen, H.-W. Wang, G. Cao, Effect of Al(OH)3 on the hydrogen generation of aluminum–water system, J. Power Sources 219 (2012) 16–21, https://doi.org/10.1016/j.jpowsour.2012.06.077.

[39] X. Chen, Z. Zhao, M. Hao, D. Wang, Research of hydrogen generation by the reaction of Al-based materials with water, J. Power Sources 222 (2013) 188–195, https://doi.org/10.1016/j.jpowsour.2012.08.078.

[40] J.P. Hamilton, C.G. Pantano, S.L. Brantley, Dissolution of albite glass and crystal, Geochim. Cosmochim. Acta 64 (2000) 2603–2615, https://doi.org/10.1016/S0016-7037(00)00388-4.

[41] C.A. Macris, R.C. Newton, J. Wykes, R. Pan, C.E. Manning, Diopside, enstatite and forsterite solubilities in H2O and H2O-NaCl solutions at lower crustal and upper mantle conditions, Geochim. Cosmochim. Acta 279 (2020) 119–142, https://doi.org/10.1016/j.gca.2020.03.035.

[42] A. Stefánsson, Dissolution of primary minerals of basalt in natural waters: I. Calculation of mineral solubilities from 0°C to 350°C, Chem. Geol. 172 (2001) 225–250, https://doi.org/10.1016/S0009-2541(00)00263-1.

[43] G. Arliguie, J.P. Ollivier, J. Grandet, Etude de l'effet retardateur du zinc sur l'hydratation de la pate de ciment Portland, Cem. Concr. Res. 12 (1982) 79–86.

[44] M. Yousuf, A. Mollah, R.K. Vempati, T.C. Lin, D.L. Cocke, The interfacial chemistry of solidification/stabilization of metals in cement and pozzolanic material systems, Waste Manag. 15 (1995) 137–148, https://doi.org/10.1016/0956-053X(95)00013-P.

[45] Q.Y. Chen, C.D. Hills, M. Tyrer, I. Slipper, H.G. Shen, A. Brough, Characterisation of products of tricalcium silicate hydration in the presence of heavy metals, J. Hazard. Mater. 147 (2007) 817–825, https://doi.org/10.1016/j.jhazmat.2007.01.136.

[46] J.F. Young, A review of the mechanisms of set-retardation in Portland cement pastes containing organic admixtures, Cem. Concr. Res. 2 (1972) 415–433, https://doi.org/10.1016/0008-8846(72)90057-9.

[47] D. Jansen, F. Goetz-Neunhoeffer, C. Stabler, J. Neubauer, A remastered external standard method applied to the quantification of early OPC hydration, Cem. Concr. Res. 41 (2011) 602–608, https://doi.org/10.1016/j.cemconres.2011.03.004.

[48] P. Lawrence, M. Cyr, E. Ringot, Mineral admixtures in mortars: effect of inert materials on short-term hydration, Cem. Concr. Res. 33 (2003) 1939–1947, https://doi.org/10.1016/S0008-8846(03)00183-2.

[49] E. Berodier, K. Scrivener, Understanding the filler effect on the nucleation and growth of C-S-H, J. Am. Ceram. Soc. 97 (2014) 3764–3773.

[50] D.P. Bentz, P.-C. Aitcin, The hidden meaning of water-cement ratio, Concr. Int. 30 (2008) 51–54.

[51] P. Hewlett, M. Liska, Lea's Chemistry of Cement and Concrete, Butterworth-Heinemann, 2019.

[52] J.W. Bullard, H.M. Jennings, R.A. Livingston, A. Nonat, G.W. Scherer, J.S. Schweitzer, K.L. Scrivener, J.J. Thomas, Mechanisms of cement hydration, Cem. Concr. Res. 41 (2011) 1208–1223, https://doi.org/10.1016/j.cemconres.2010.09.011.

[53] K.L. Scrivener, T. Füllmann, E. Gallucci, G. Walenta, E. Bermejo, Quantitative study of Portland cement hydration by X-ray diffraction/Rietveld analysis and independent methods, Cem. Concr. Res. 34 (2004) 1541–1547, https://doi.org/10.1016/j.cemconres.2004.04.014.

[54] B. Lothenbach, G. Le Saout, E. Gallucci, K. Scrivener, Influence of limestone on the hydration of Portland cements, Cem. Concr. Res. 38 (2008) 848–860, https://doi.org/10.1016/j.cemconres.2008.01.002.

[55] G. Le Saoût, B. Lothenbach, A. Hori, T. Higuchi, F. Winnefeld, Hydration of Portland cement with additions of calcium sulfoaluminates, Cem. Concr. Res. 43 (2013) 81–94, https://doi.org/10.1016/j.cemconres.2012.10.011.

[56] D.P. Bentz, S. Remond, Incorporation of Fly Ash into a 3-D Cement Hydration Microstructure Model, US Department of Commerce, Technology Administration, National Institute of …, 1997.

[57] S. Mindess, J.F. Young, D. Darwin, Concrete Prentice-Hall, Englewood Cliffs, NJ 481, 1981.

[58] A.M. Neville, Properties of Concrete, Pitman, 1973.